ISSN 1999-530X

Volume 1 Number 1 January 2009

JEAS

JOURNAL OF ENGINEERING AND APPLIED SCIENCE

Rajshahi University of Engineering & Technology
Bangladesh

Journal of Engineering and Applied Science
Editorial Board

Rajshahi-6204, Bangladesh.
director_re_ruet@ruet.ac.bd

Journal of Engineering and Applied Science

Volume 1, No. 1
May 2009, Maiden Issue

Editorial

In order to facilitate and promote postgraduate studies and research Bangladesh Institute of Technology (BIT), Rajshahi (former Rajshahi Engineering College) was upgraded to Rajshahi University of Engineering & Technology (RUET) in September 2003. Since then, M.Sc/M. Engineering, M. Phil and Ph.D. degrees are being offered, research activities carried out; knowledge created and exchanged in different fields of engineering and science. It is necessary that the knowledge and experiences are shared in wider educational communities. Such dissemination not only informs the stakeholders but also establishes the position of the university in terms of its academic and research perspectives. With this objective the *Journal of Engineering and Applied Science (JEAS)* is launched with the publication of its first issue which is in your hand now.

The JEAS is a multi-disciplinary academic publication which seeks to adopt an integrated approach to the discussion of issues related to engineering and applied science. Thus the journal provides a platform/ forum/ outlet for publication of articles in different areas of engineering and science, such as civil, electrical, mechanical, computer science and engineering, electronics and telecommunication, industrial and production engineering, chemistry, physics and mathematics.

This maiden issue of the *Journal of Engineering and Applied Science* consists of seven papers on diverse themes and topics. The manuscripts were reviewed by a pool of experts from various disciplines within and outside the editorial board. We hope that you will find the papers selected for this maiden issue of the journal invigorating reading. Expected readership includes teachers, students, researchers, professionals and practitioners as well as policy makers. We are very receptive to new and constructive ideas that will go a long way in improving the quality of the journal. Since our intention is to publish two issues per volume annually, we shall continuously accept submissions.

Professor Dr. M. F. Bari
Editor-in-Chief

Temperature Dependence of Microwave Absorptions of Bi2212 Single Crystals under Parallel Fields

Ajay K. Sarkar[1,*], T. Endo[2], M. R. Amin[1], M. S. Hossain[1]
[1]Department of EEE, RUET, Rajshahi-6204, Bangladesh,
[*]Email: akrishnosarkar@yahoo.com,
[2] Department of EEE, Mie University, Tsu, Mie514-8507, Japan.

Abstract

Temperature dependence of Microwave Absorptions (MA) of Bi2212 HTS single crystals for Ha//ab was measured. The first peak intensity of the MA spectra decreases with increasing temperature, indicating that the out of plane surface screening current for parallel fields decreases with temperature. The penetration of Josephson vortex in between the superconducting planes becomes much easy with increasing the temperature. Then the decoupling of the superconducting planes (CuO_2) is enhanced with the increase in Josephson vortex density inside the sample with increasing temperature. It is observed that the first peak position is shifted to the lower field side with increasing temperature. This is due to the suppression of the Meissner state with increasing temperature. The phase diagram for Bi2212 for Ha//ab was proposed in this work.

Keywords: Bi2212 HTS single crystal; MA spectra; Surface Screening Current; Josephson Vortex; Meissner State

1. Introduction

The field of superconductivity has grown so rapidly in recent years that it is difficult to predict even the short-term impact of High Temperature Superconductors (HTS) on fields as far-ranging as computers and infrared detectors. The most important application areas of HTS materials are microelectronics components, superconducting wires, cables, and magnets. In microelectronics applications require superconductors typically in the form of thin films, whereas other applications are mainly realized using bulk superconductors. Microelectronics devices make use of high-temperature superconductors for two reasons. First, it is possible to design and construct sensitive detectors, e.g., for measuring magnetic flux or mm-wave radiation. Secondly, HTS materials could be used to replace existing designs based on normal conductors. Compared to conventional devices, HTS components can be significantly reduced in size while their performance is improved. Because, in principle, there are no electrical losses and power consumption in the components. High-temperature superconducting microwave components including filters, antennas, resonators, and transmission lines are amazing applications of HTS materials.

Among these applications, HTS tunable microwave filters possess urgent demand in communication fields due to their low microwave loss compared with normal metals. These HTS tunable filters will be the most expected devices for the base stations of mobile phone system for the next generation. They must be composed of double layers of HTS and Ferromagnetic thin films and work under magnetic fields. Then it is necessary to investigate microwave properties, especially MA on HTS single layers, HTS/Ferro double layers and multilayers under the applied magnetic fields (Ha).

Fortunately, immediately after the discovery of HTS materials, intense nonresonant microwave and rf signals [1-2] were discovered in these materials. The technique of microwave absorption (MA) is very useful in characterizing superconductors because the MA is related to important fundamental superconducting phenomena such as penetration of magnetic flux, vortex motion, critical shielding current, critical Josephson state and entrance of fluxons into current loops [3-7].

In this work MA measurements were conducted on Bi2212 single crystals under **parallel** fields applied to the superconducting CuO_2 plane. The Results obtained from the measurement were interpreted by screening current features and vortex dynamics in the samples.

2. Experiment

2.1. Procedure of microwave absorption measurement

Microwave absorption (MA) is measured with a renovated electron spin resonance (ESR) device as shown in Figure 2.1. The sample is placed in TE102 mode cavity and it is zero fields cooled at a temperature less than the transition temperature T_C using liquid nitrogen. The microwave propagated from the klystron is introduced into the resonant cavity by a wave guide (Figure 2.1), and under the resonance condition a standing wave is formed in the cavity. The sample is placed at the center of the cavity where microwave magnetic field (H_W) is the largest, and microwave electric field (E_W) is minimum (or zero). However, when the sample absorbs microwave, the resonance condition collapses, and microwave is reflected from the cavity. The reflected wave is detected by a diode microwave detector and the amount of absorption is measured. The measured signal by the diode detector is amplified by the pre-amplifier (pre-amp). Then modulated MA signal (S) is obtained upon phase sensitive detection at the fundamental of modulation frequency using a lock-in amplifier system. The output of the detector is fed to the lock-in amplifier system. The quasi-static magnetic field (Ha) is applied to the sample and is slowly swept upward and downward. This is called "The DC field" or "the field" simply hereafter. The modulation field Hm is superimposed on the DC field Ha in the same direction at high frequency of, say, 100 kHz for obtaining the sensitive modulated MA signal. Therefore, the signal recorded with the recorder is Modulated Microwave Absorption (MMA) signal.

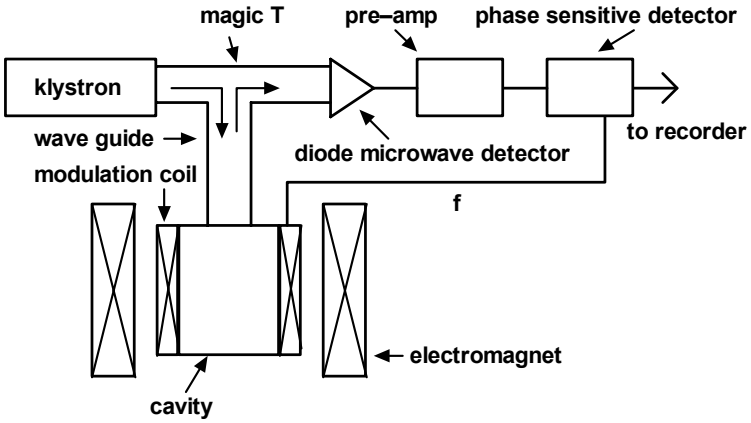

Figure 2.1. Set up of ESR apparatus for MA measurement

2.2. Sample preparation methods

The Bi2212 single crystals were grown by self-flux method using alumina crucible. The stoichiometric quantities of $CaCO_3$, $SrCO_3$ and CuO powders (99.99% purity) were mixed thoroughly and then sintered at 820°C for 48 h and cooled down to room temperature and then grounded. Bi_2O_3 powder was then added to the ground material and the mixture was heated in the alumina crucible. The heating schedule for synthesis of Bi2212 single crystal was as follows. First sample is heated at 120°C/h to 880°C, then 31°C/h to 1005°C and soaked for 4 h. Then it is cooled at 20°C/h to 920°C. Sample is cooled at a very slow rate of 0.5°C/h to 870°C. Again it is cooled further to 760°C at 1°C/h and then by furnace cooling to room temperature. Single crystals were separated by breaking the alumina crucible.

2.3. Sample cooling method

A diagrammatical view of the liquid nitrogen cryostat is shown in Figure 2.3 that was used in the experiments. The sample was put into a sample tube and the tube is put in a dewar filled with liquid nitrogen then the sample is cooled at liquid nitrogen temperature of about 77 K. The tip of a sample tube is closed with a seal stopper.

2.4. Measurement method of sample temperature

The sample temperature is measured by a copper - constantan thermocouple (Figure 2.4) In case of field sweep experiment, the temperature of the sample is measured before the sweep. In case of fixed Ha the copper-constantan thermocouple is attached to the sample then the precise sample temperature (T) could be directly monitored during the absorption measurement. The coolant temperature is naturally increased with time as atmospheric oxygen is gradually dissolved into the liquid nitrogen.

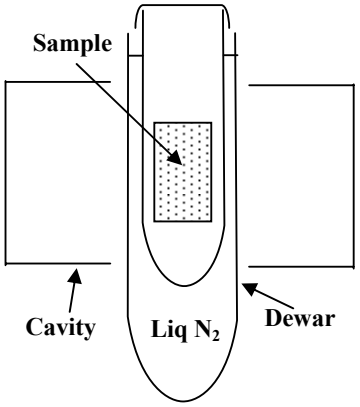

Figure 2. 3. Cooling process of sample by liquid nitrogen

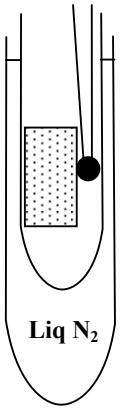

Figure 2. 4. Method of sample temperature measurement

3. Result and Discussion

3.1. The critical temperature

The critical temperature (T_C) of the sample was estimated from the microwave absorption signal vs temperature using continuous temperature dependence of microwave signal (Figure 3.1). The sample shows no absorption signal above 86.5 K, a sharp increase is observed indicating the T_C = 86.5. The sharp transition width indicates that the single crystal quality is of reasonably good.

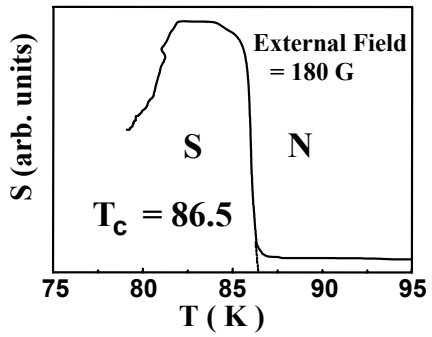

Figure 3.1. MA signal S vs T for Bi2212 single crystal at an external applied magnetic field of 180 G. The T_C is obtained as 86.5 K.

3.2. MA spectra at different temperatures

The reentrant phase diagram proposed by Fisher is for perpendicular field configuration. Hashizume et al. [8] verified the reentrant phase experimentally by the temperature dependence of MA for perpendicular field configuration using MA technique. For Ha//ab plane authors measured only at around 80 K and showed the simple line shape of MA for this configuration with the absence of broad peak.Auhors found that only a single first peak is present near zero fields, which is wider than the first peak for the perpendicular field configuration. Rastogi et al. [9] also reported the same characteristics for this field configuration. However, no phase diagram is reported so far for this case. Furthermore, the widening of the first peak must have some meaning characteristics, which has not been reported so far. In this work, we measured temperature dependence of MA

for Ha//ab. It shows MA spectra (S) at different temperatures (T) for Ha//ab (Figure 3.2). The label G stands for the gain of the receiver at that particular measurement. The microwave power in this experiment was 0.5 mW. The solid and dashed lines in the spectrum indicate the upward and downward field sweep respectively.

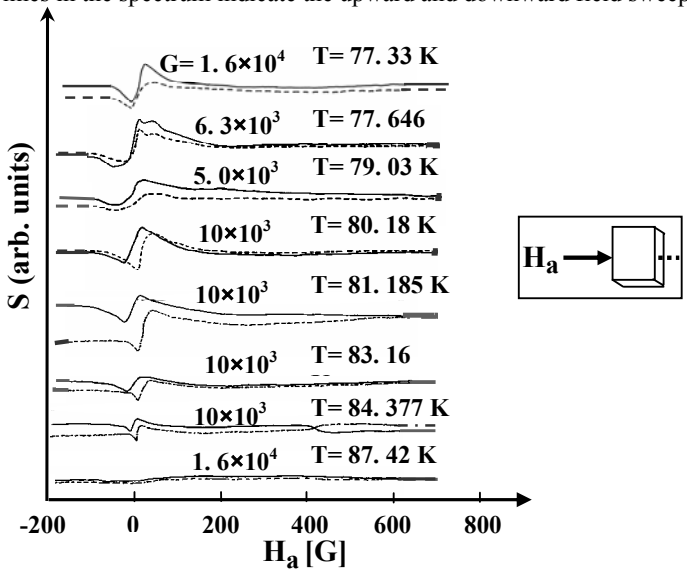

Figure 3.2. T-dependence of MA for Ha//ab.
Inset figure shows applied field direction to the sample.

3.3. First peak signal intensity at different temperatures

From the spectrum in Figure 3.2, it seems that MA signal intensity decreases with increasing temperature. Then the first peak signal intensity S_{p1} was plotted as a function of temperature (T) in Figure 3.3.

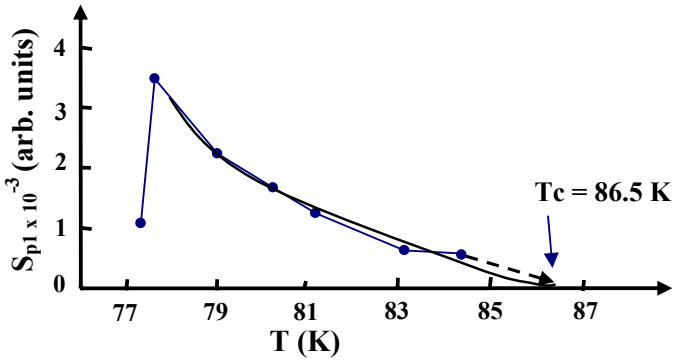

Figure 3.3. Temperature (T) vs normalized peak to peak intensity of first peak

The first peak intensity decreases with increasing temperature, indicating that the out of plane surface screening current for parallel fields decreases with temperature. The penetration of Josephson vortex in between the superconducting planes becomes much easy with increasing the temperature. Then the decoupling of the superconducting planes (CuO_2) is enhanced with the increase in Josephson vortex density inside the sample with increasing temperature. The T_C of this sample, which was obtained form the continuous temperature dependence of MA signal for Ha//c has also been confirmed by this experimental result. As MA signal is zero for 87.42 K (Figure 3.2), so T_C lies somewhere between 84.377 K and 87.42 K. The extrapolation of the curve in Figure 3.3 gives a value of 86.33 K which is almost the same with the value of 86.5 K obtained from MA spectrum in Figure 3.1.

3.4. First peak position at different temperatures (T)

The widening of the first peak for Ha//ab compared with Ha//c found by Hashizume et al. [8] must indicate

something about the Meissner state. The author of that paper did not mention any behavior with this connection. Then from the present experimental results (Figure 3.2) the first peak positions Hp1 of MA signals are plotted as a function of Temperature as shown in Figure 3.4.1.

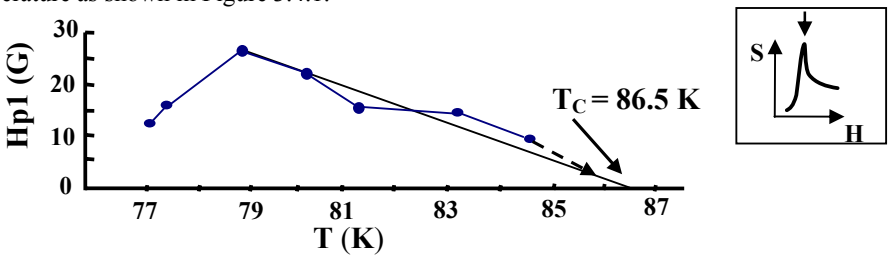

Figure 3. 4.1. First peak position vs temperature. Inset describes the definition of Hp1.

It is observed that the first peak position is shifted to the lower field side with increasing temperature. This is due to the suppression of the Meissner state with increasing temperature. From these plotting, the phase diagram for Ha//ab can be proposed as shown in Figure 3.4.2. The phase diagram proposed in Figure 3.4.2 for Ha//ab contains no reentrant liquid state (L_1) and Solid state (S) due to the absent of Dip and broad peak in MA spectrum for this field configuration.

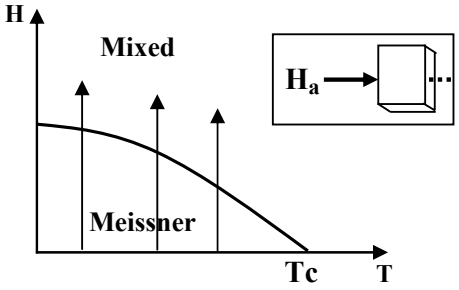

Figure 3.4.2. Schematic phase diagram for Ha//ab. Inset shows applied field orientation.

3.5. Meissner state for parallel and perpendicular field configuration

Comparison of the Meissner state for this field configuration with that of the reentrant phase diagram for Ha//c indicates that the H_{C1} line for Ha//ab is located at higher fields than for Ha//c. So Meissner state evaluated by MA is extended at higher fields for Ha//ab than for Ha//c as shown in Figure 3.5.

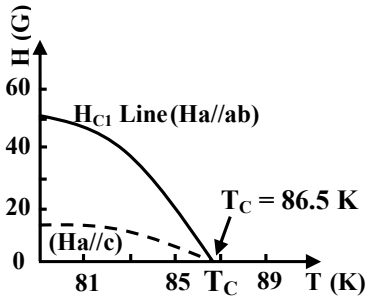

Figure 3. 5. Comparison of the Meissner state for Ha//ab and Ha//c.

4. Conclusions

The temperature dependence of Microwave Absorption (MA) of High T_C Superconductors (HTS) of Bi2212 was measured to characterize them for their application in the microwave devices. Bi2212 single crystals have high T_C, desirable for the device fabrication. The temperature dependence of MA spectra of Bi2212 under the parallel fields to the superconducting plane (Ha//ab) (Josephson configuration) shows very simple and monotonous features with the variation of temperatures even up to T_C. The spectra includes only the wider first peak at all the temperatures, there is no broad peak and Dip unlike the temperature dependence of MA for perpendicular fields to the plane (Ha//c) (Abrikosov configuration). A phase diagram can be proposed for Josephson configuration from those results. It is observed that the boundary line of the Meissner state, H_{c1} is located at higher field for Josephson than for Abrikosov configuration. These results are originated from the widening of the first peak for Ha//ab compared with Ha//c.

Acknowledgments

The authors would like to express their intense gratitude, thanking and appreciation to Dr. Hong Zhu,(Professor, Department of Physics, University of Science and Technology of China), Post Doc. Fellow and former Masters student Takahisa Sakurada in Professor Endo's Laboratory for their very big hand in solving various experimental problems while working in Endo's laboratory.

References

[1] S.V. Bhat et al., "Absorption of electromagnetic radiation by superconducting $YBa_2Cu_3O_7$: an oxygen-induced phenomenon", *J. Phys.* C **20**, L559, 1987.

[2] S.V. Bhat et al., "An 'EPR' study of YBa2Cu3O7 and related high-temperature superconductors", *Pramana J. Phys.* **28**, L425, 1987.

[3] E. J. Pakulis et al., "Microwave absorption studies of Y-Ba-Cu-O", *Phys. Rev. B* ***37*****,** 5940, 1988.

[4] R. Karim et al., "A study of hysteretic absorption in polycrystalline high-T_c superconductor YBCO", *IEEE Trans. Mag.* **26**, 1439, 1990.

[5] K. W. Blazey et al., "Microwave Study of the Critical State in High-T_C Superconductors", *Solid State Commun.* **65**, 1153 1988.

[6] Y. Maniwa et al., "Mechanisms of direct microwave absorption in $Y_1Ba_2Cu_3O_{7-x}$", *Phys. C* **156**, 755 (1988).

[7] K.N. Shrivastava, "Microwave Absorption in High-Temperature Superconductors", *Physica Status Solidi (b)* **164**, K51 (1991).

[8] A. Hashizume et al., "Microwave Absorption Spectrum and reentrant phase in Bi2212 Single Crystal: Temperature dependence", *Physica C: Superconductivity,* **378-381, Part 1**,474 (2002).

[9] A. Rastogi et al., "Nonresonant microwave absorption study of intrinsic Josephson coupling in $Bi_2Sr_2CaCu_2O_8$ single crystals" *Phys. Rev. B* **53**, 9366 (1996).

Development of Gameplay Engine for Real Life First Person Shooter Game

A. B. M. Hamidul Islam[1], Md. Shahid Uz Zaman[2], Shamsuddin Shahid[3]
and Md. Hafiz Uddin[4]
[1]Assistant Professor, Department of EEE, AUST, Talaimari, Rajshahi-6204, Bangladesh
[2]Professor, Department of CSE, RUET, Rajshahi-6204, Bangladesh
[3]Assistant Professor, Department of Applied Physics & Electronic Engineering, RU, Rajshahi-6205, Bangladesh
[4]IT Professional, Customs, Excise &VAT, Commissionerate, 248/2, Upasharar, Rajshahi-6202, Bangladesh
Email: mhamidulbd@yahoo.com, szaman22@yahoo.com, sshahid@ru.ac.bd, hafiz012001@yahoo.com

Abstract

In order to increase the playability of a computer game, the gameplay engine should be simple and efficient. This paper presents a simplified design approach of gameplay engine for the implementation of first person shooter game. A three-dimensional first person shooter game named as "The Dominator" has also been developed using the proposed gameplay engine. The functions of the gameplay engine are discussed in the context of the game-The Dominator.

1. Introduction

A game engine is a software system designed for the creation and development of computer game. Gameplay is the core game-making algorithm of game engine, which calls the different functions of the different engines, such as graphics engine, sound engine, physics engine, user interface engine, intelligence module as well as other engines and modules of the game engine according the design of a particular game [1-3]. A well-known subset of game engines are 3D first-person shooter (FPS) game engines. In this present paper, a simplified design approach of gameplay engine for the implementation of a three-dimensional first person shooter game has been proposed.

2. Key Elements of Gameplay Engine

The key elements of gameplay engine are[4,5]: (i) game mechanics which defines all controls and interactions within the game; (ii) experience duration which defines the average time requires to complete teach stages, levels and missions of the game; (iii) subsidiary effects that include visual, aural and decorative effects; (iv) useful rewards which include new game modes, upgrades etc. that entices users to continue playing the game; and (v) difficulty that defines how hard it is to pass obstacles and non-playing characters.

3. Implementation Details of Gameplay

The main task of gameplay is to interface levels, actors and artificial intelligence with game engine [6]. The gameplay engine of *The Dominator* [7] does this by using four modules namely *CTF*, *TGLoading*, *UI* and *HUD* and five classes namely *Centity_Player*, *CTEntity_CTFAgentManager*, *CTEntity_DomAgent*, *CTEntityVarious* and *CTMD3*.

In *CTF* module the *Centity_Player*, *CTEntity_CTFAgentManager*, *CTEntity_DomAgent*, *CTEntityVarious* and *CTMD3* class variable are declared and defined. In this module, *SetAnimation* function is also declared and defined for all actor animation.

In *UI* module, algorithms of all User-Interface pages, buttons, labels, picture boxes and edit boxes are defined. The rendering process of these controls under UI engine is shown in Figure 1. In *UI* module rootpage page window and its components are declared first. This page is loaded by calling *LoadRootPage* function. Then *LevelPage* page window, *ControlPage* page window, *PlayerInfoPage* page window, *CreaditPage* page

window, *HelpPage* page window and *ExitPage* page window are loaded along with their components by calling *LoadLevelPage*, *LoadControlPage*, *LoadPlayerInfoPage*, *LoadCreaditPage*, *LoadHelpPage* and *LoadExitPage* functions respectively. These functions are called by using Loading function of *TGLoading* module. These pages are rendered when their associated button are clicked in the rootpage. For this purpose, *UI_HandleEvents* handle function is called by using the *SequenceLoad* function of the *TGLoading* module.

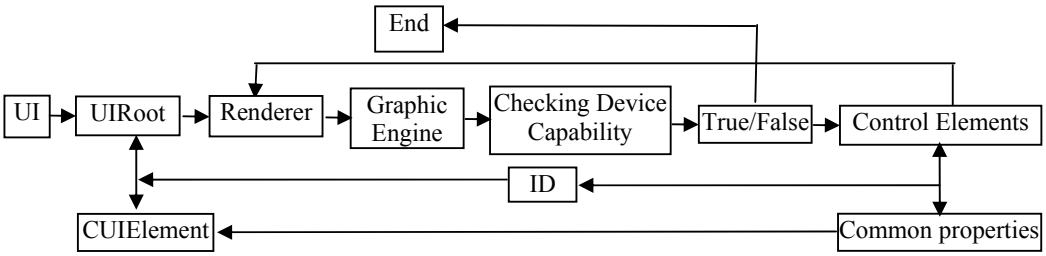

Figure 1. Rendering process of UI engine

HUD module is used to display all the information of game player and his opponent in the game. For this purpose, in *TGLoading* module, global variables of different class module of game engine are declared first. These modules are set before initialization of the window. After loading the game engine, other components such as input, camera, world, octree, DirectX variable and sound engine components are loaded by calling *DXLoding* functions. Subsequently, the *SequenceLoad* function is called which is the root looping rendering function. In this function all the game engine rendering functions of *The Dominator* is called between *BeginRender* and *EndRender* functions of graphics engine. First the graphics engine is called for rendering window. Next, the User-Interface (*UI*) engine is called. After obtaining different information of the game from UI engine, it calls the Step6Loading function. This function calls the camera *ComputeWorldViewMatrix* function, skybox rendering function *RenderSky* and octree level data rendering function *Render* from game engine world class module, Finite State Machinge (*FSM*) rendering function from *CTEntity_CTFAgentManeger* class module, different entity rendering function *RenderEntity* from *CTEntityVerious* class module and *HUD* rendering function *HUD_Render* from *HUD* module. The *CTEntity_CTFAgentManager* class maintains actor and artificial intelligence information. Its *Load* function is called in the *LevelDataLoading* function of *TGLoading* module. In this function, it loads level path information as well as friend and enemy actors by calling *Init* function of *CTEntity_DomAgent* class module. The render function of *CTEntity_CTFAgentManager* calls *CTEntity_DomAgent* render function for rendering actor with path finding and *FSM*. The working process of FSM system to implement AI is shown in Figure 2. It also calls render function of the *CEntity_Player* to render person to play the game as well as *IsSeeBox*, *AddPlayerHealth* and *SetTime* function to check the gameplay time period. At the end of time period, it displays the result depending on the points obtained by each side.

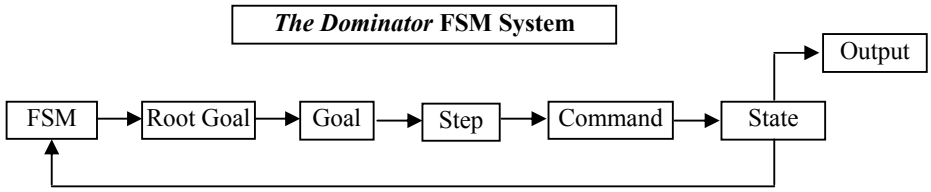

Figure 2. Working process of AI in *The Dominator* by using FSM

In *CTEntity_CTFAgentManager*, *IsSeeBox* function checks the distance between the domination point and an actor or a player. If he is within 80 cm, the point or region is set on his capture. It also checks the time period of capture. If it exceeds 20 seconds it gives three points to the capturing side. Its *AddPlayerHealth* function is used to add heath to a player when he touches the box.

In *CTEntity_DomAgent* class all the *FSM* development algorithm is written. Create function of *CTEntity_DomAgent* class creates root goals, goals under each root goals, steps under each goal, command under each steps and send these information to the game engine *CFSM* class. The *m_fsm_GoalChangeLogic* function of *CTEntity_DomAgent* holds the algorithm to check whether a goal is changed and executed or not. The *m_fsm_NextStepSelection* function executes steps and commands of a goal. Its *EnumerateEnemies* function gives the information of friend or enemy. This is done by checking the identification number of the actors.

In the proposed game four goals have been developed, which are Dominate, Health, Guard and Attack. Beside these, three commands viz. *SCRIPTCOMMAND_GOTOPOINT*, *SCRIPTCOMMAND_GOTOPOINT_WITHCOLLISION* and *SCRIPTCOMM AND_STAY* have been developed.

When an actor is loaded for rendering, it is assigned a default root goal named "Domination" and a goal to "Dominate". In this goal, actor find a free domination point by calling the *Free_Dom function*, a free health point by calling the *Free_HealthPos* function, a Free Guard point by calling the *Free_Guard* function, and action position by calling the *ActionPos* function. If any step of any goal fails, it calls *RandomPoint* function to go any random point. If the actors of a side capture all the domination points then it goes to Gurard goal by calling *m_fsm_GoalChangeLogic* function. If it finds any enemy, it enters into the Attack goal and calls Fire function from *CEntityVarious* class. Each goal has different functions to switch from one goal to another. These information send to *CFSM* class for managment and calculation by *Update* function. The *CFSM* module also finds shortest path by calling *CTAI* class module to move the actor from his position to the target point.

The render function of *CFSM* module also checks if the player mode is false or not as the artificial intelligence is applied for non-playing actors only. It also checks the Deadstate (*m_deadState*) variable. If it is greater than 0, it calls *RenderDeathState* function, which render dead actor animation to show the dying action of the actor on the geometry for two seconds and then regenerates the actor in the regeneration position. The regeneration position is found by calling the *GetReInitilizePos* function of the *CTEntity_CTFAgentManager* class. Then it sets the regenerate actor *Deadstate* to 0 and assign Dominate goal. *RenderModel* and *Weapon_Render* functions are called to render the actors with their weapon. If *Deadstate* is 0, it calls the *Update* function to send current information of the actor to *CFSM* module of the game engine. Then it calls *RenderModel*, *Weapon_Render* and *SetAnimation* functions to animate each actor. If the player mode is true, it renders a camera as a player instated of an actor to which actor player mode is assigned. *CliveObjects_MakeDamge* function is called when a bullet intersects an actor. It decreases health of the actor. If its health is 0, it checks whether he was in actor side or player side.

In *CEntity_Various* class, *LoadEntities* function calls the *LoadDominentPointEntity* function to find and load domination point, *LoadHealthPointEntity* function to find and load Health point, *LoadDeadActorInitPos* function to load reinitialized point of each side, *LoadSLRGun* function to load the *SLR* gun model.

RenderEntity function calls *RenderDominentPointBox* and *RenderHealthPointBox* functions. *RenderDominentPointBox* function is used to render domination point flag. *RenderHealthPointBox* function is used to render the health box when its render property is true. If render property of the box is false, it counts 10 seconds and reset its render property true.

The Fire function is used to fire bullet. It also checks whether the bullet intersects the target actor or not. If it intersects target actor, it calls the *CliveObject_Damage* function of the *Centity_DomAgent* class to take target actor index as its arguments. The *DrawBulletRay* function is used to draw red line from firing actor position to the target actor position.

The *CTMD3* class module is used to load and render domination point flag model because we used md3 format model for it. In *CTMD3* class module *OpenMD3File* function is used to load the md3 format data. The render function is used to render md3 format model with animation by calling MD3UpdateAnimation function. The start and end frame of current animation of the model is assigned by calling the PlayAnimation function.

4. How the Game Works

The working cycle of game engine and gameplay is shown in Figure 3. First, the game engine calls graphics engine for detecting and managing graphics card capabilities. The graphics engine runs different sub routine to check whether the graphics card has the capabilities to support all the properties that is required to run the game. If it supports all the properties then it makes 3D rendering environment in the currently defined form, otherwise it exits from the application. This process of the game is called Initializations.

After Initializations, the gameplay engine calls the user-interface engine of the game engine. The user interface engine contains all the information about the game. From user interface engine the user can start to play the game by clicking the play button of *LevelPage* page window.

When the user click play button the gameplay engine calls the level and actor loading modules to load the level and actor data. Game engine then render these data. Next, the gameplay engine calls the camera and keyboard module of the game engine. The camera is used to show the particular area of the level and keyboard is used to move the camera from one location to another location in the level. The game engine then calls the culling module to truncate rest of the area that is not visible in the camera.

The gameplay then calls the path finding and artificial intelligence to interact with the rest of actor. The artificial intelligence is implemented in the game by using the *FSM* tools. The *FSM* calls path finding to find the path of an entity to move from one position to other. It then calls the collision detection and gravity module which are used to prevent collision with rigid body and keep the actors with level geometry respectively.

The *FSM* system manages these routines for the actors and the players. If the actors of one side encounter the actors of player side, *FSM* system calls the weapon manager module and fires the opponents. If the bullet

intersects the actors or player, *FSM* decreases intersected actors or player health. This process is continued until the player exit from the game or the playtime is over.

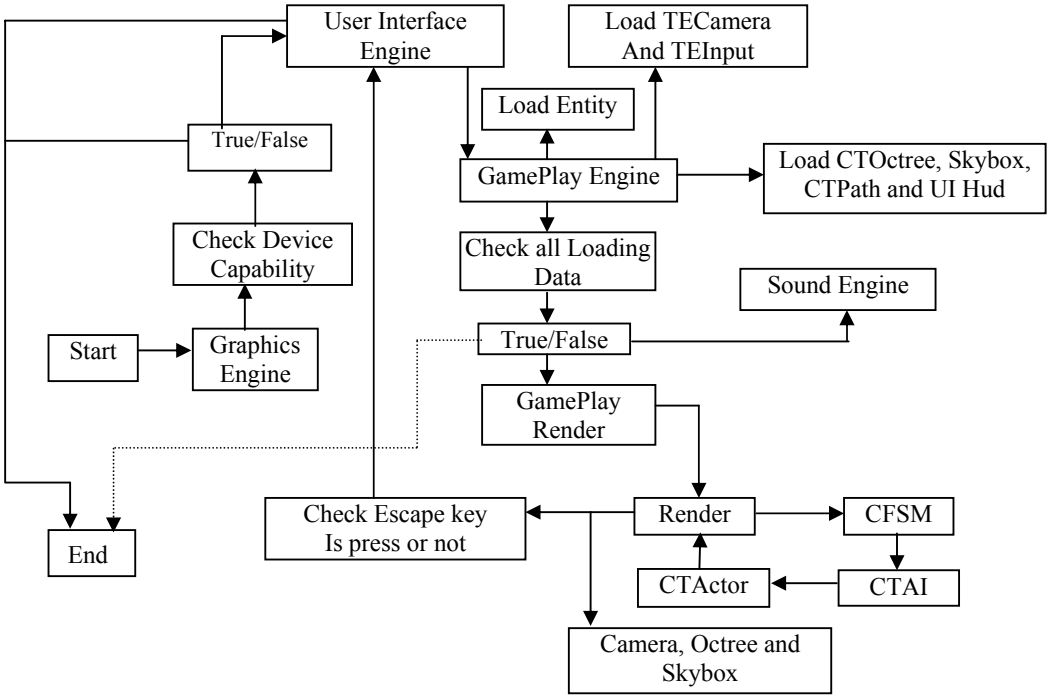

Figure 3. Working cycle of the game engine and the gameplay engine

5. Conclusion

A game engine is termed as 'good' if it gives flexibility in making the game and at the same time if it supports all the key features of a game. In the present paper a simplified design approach of Gameplay engine has been proposed. The proposed approach is discussed through the implementation of a three-dimensional first person shooter game. Similar approach can be used in designing of any other types of computer game.

References

[1] André L., Tricks of the 3D Game Programming Gurus-Advanced 3D Graphics and Rasterization, Pearson Education, pp. 1728, 2003.

[2] Andrew M. and Teijo H., Developer's Guide to Multiplayer Games, Wordware Publishing, pp. 589, 2003.

[3] Daniel S. C., Dalmau and Daniel S. C., Core Techniques and Algorithms in Game Programming, McGraw-Hill Osborne Media, pp. 368, 2003.

[4] DeLoura M., Game Programming Gems, Charles River Media, pp 600, 2000.

[5] Erik B., Game Development, Wordware Publishing, pp. 432, 2003.

[6] Francois D. L., Game Design Perspectives, Charles River Media, pp.420, 2002.

[7] A. B. M. Hamidul Islam, Shamsuddin Shahid and Md. Mortuaz Ali "Design and Development of a Real-Life Game", National Conference on Electronics, Information and Telecommunication, Bangladesh. Vol No. 984-300-000645-7, pp. 167, June, 2007.

Synthesis, Characterization and Biological Screening of the Metal Complexes with Cyanex 301 and Cyanex 302

Tarun Kumar Pal and Md. Ashraful Alam
Department of Chemistry, Rajshahi University of Engineering & Technology, Bangladesh

Abstract

A new complexes of zinc(II), cadmium(II) and mercury(II) with new organic ligands viz Cyanex 301[i.e., bis(2,4,4-trimethylpentyl) dithiophosphinic acid] and Cyanex 302 [i.e., bis(2,4,4-trimethylpentyl) monothio-phosphinic acid] of the types [ZnL_2], [ZnL'_2], [ML_2].H_2O and [ML'_2].H_2O [M=Cd(II) and Hg(II)], have been prepared and characterized by elemental analysis, molar conductance, IR and UV/VIS spectroscopy as well as magnetic measurements. The spectra of the complexes suggested that uninegative bidentate coordination of Cyanex 301 and Cyanex 302 ligands to the metal ions. According to obtained data, the complexes of divalent metal ions are tetrahedral geometry and non-electrolytes. The antibacterial and antifungal activities of the ligands and their metal complexes have been also investigated against six pathogenic microorganisms. The complexes have shown good antibacterial and antifungal activities.

Key words: Cyanex 301, Cyanex 302, IR, Antibacterial, Antifungal and DMSO.

1. Introduction

Metal ions play a vital role in a vast number of biological processes. The ions with biologically active ligands are a subject of considerable interest. Some of the biologically active compounds act *via* chelation. The antimicrobial activity could be mainly due to the structure of the complexes and also the oxidation state of the metal ions. Transition metal ions are known to form chelates with various polydentate ligands [1]. However, complexes of these metal ions with organic ligands *viz* Cyanex 301 and Cyanex 302 are lacking. So, a study has been made with such complexes. The derived knowledge will be helpful for solvent extraction of the metal ions [2]. The preparation and characterization of some complexes of Cyanex 301 and Cyanex 302 with metal ions *viz* Zn (II), Cd (II) and Hg (II) have been reported in this paper. Literature studies showed that complexes of various metals with different ligands are of great importance, because many of them are efficient stoichiometric and catalytic reagents. These complexes have been extensively used in the therapeutic, analytical, biological, industrial fields and coordination chemistry [3]. In view of the above discussions it has been planned to synthesize and characterized of Zn (II), Cd (II) and Hg (II) complexes with the ligands to deduce their structure by various techniques such as elemental analysis, molar conductance, electronic spectra, magnetic susceptibility and infrared studies. The antibacterial and antifungal activities of the ligands and their metal complexes have also been carried out.

2. Materials and Methods

2.1. General procedure for the synthesis of metal complexes

A solution of the ligand Cyanex 301 or Cyanex 302 (1 mmol) in absolute ethanol (25 ml) was added to a solution of potassium hydroxide (1 mmol) in absolute ethanol (25 ml) and the mixture was stirred well and heated on a water bath for about 30 min to reduce it to half volume. The resulting mixture (potassium salt of Cyanex) was allowed to stand at room temperature. Then a solution containing 0.5 mmol of the required metal chloride salt in absolute ethanol (20 ml) was slowly added to the above potassium salt of Cyanex solution, with stirring at room temperature. The metal complex was formed immediately. The mixture was stirred for several minutes. The product was removed by filtration, washed several times with cooled absolute ethanol, then with distilled water (to remove KCl formed) and finally dried and stored in a vacuum desiccator.

2.2. Measurement techniques

IR spectra (4000-400 cm^{-1}) were recorded on a Nicolet 310 FTIR (Belgium) spectrometer with a KBr disk and UV-Visible spectra were recorded on a 1650 PC, Shimadzu spectrophotometer in DMSO. Magnetic

susceptibility measurements were obtained with a Sherwood Scientific Magnetic Susceptibility Balance at room temperature. The electrical conductivities of 10^{-3} M solution in DMSO were carried out on a heavy-duty conductivity /temperature meter (USA), Extech Instruments, model No. 407303. Elemental analysis (C, H) was carried out with a Perkin Elmer 2400 II, organic elemental analyzer, Japan. The antibacterial and antifungal activities were also carried out against the bacteria *viz Escherihia coli, Staphyloccocus aureus* and *Salmonella typhi* and the fungi *viz Aspergillus niger, Fusarium oxysporum* and *Trichophyton sp.* by disc diffusion technique [4, 5].

3. Results and Discussion

3.1. General physical characterization

The reaction of Cyanex ligand with various metal ions [M= Zn (II), Cd (II) and Hg (II)] led to the formation of the complexes **1-6**, in the presence of alcoholic potassium hydroxide. All the complexes were obtained via the formation of a potassium salt of the Cyanex ligand. The complexes **1-6** were formed in a ligand to metal ion molar ratio of 2:1 molar ratio. All the complexes were more air stable and insoluble in most common solvents except benzene and dimethylsulphoxide. The elemental analyses and metal estimation data (Table 1) were in good agreement with their proposed formulae. The molecular mass determination of the complexes (by cryoscopic method) also supported their proposed molecular formulae. The room temperature molar conductance values of the complexes suggested that the complexes **1-6** are non-electrolyte in nature [6].

3.2. Infrared spectra

The most important IR data for the ligands and their corresponding Zn (II), Cd (II) and Hg (II) complexes have been depicted in Table 2. The free ligands showed two bands at 2868 and 2956 cm^{-1} for the aliphatic alkyl moeity, which assigned to ν (C-H) symmetric and asymmetric stretching vibration respectively. These bands are also present in the spectra of the metal complexes as expected, indicating that it was not involved in the coordination. The ν (P=S) stretching band for the ligand (Cyanex 301) was found at 637 cm^{-1} [7, 8]. This stretching band shifted in the lower frequencies in the spectra of the all complexes, which suggested the strong chelation. The infrared spectrum of the ligand showed a medium band at 2638 cm^{-1} which was assigned to ν (S-H) vibration [9]. The absence of ν (S–H) band, as well as the presence of ν (M–S) band in the complexes in the 407-411 cm^{-1} region [9], suggested the coordination of the Cyanex 301 anion to metal ions *via* sulphur atoms.

On the other hand, the IR spectrum of the free ligand (Cyanex 302) showed ν (P=S) band at 634 cm^{-1} [7,8] and ν (O-H) of P-OH moiety band at 2343 cm^{-1} [10]. A band observed in the spectrum of the ligand at 634 cm^{-1} was shifted to lower frequencies in the spectra of all complexes, which suggested the participation of thiophosphoryl sulphur atom in bonding. Band due to ν (O-H) stretching band was not observed in the spectra of the complexes. Further, the IR spectra of all the complexes exhibited two new bands in the region at 408-418 cm^{-1} [9] and 506-512 cm^{-1} [11]. These two new bands assigned to ν (M-S) and ν (M-O) respectively. In the case of water containing compounds, a band at around 3370-3449 cm^{-1} corresponding to the ν (O-H) mode [3]. Except Zn (II) complexes, all the complexes showed a broad band at 3370-3440 cm^{-1}, which indicated the presence of water molecule outside the coordination sphere [3, 12]. In the present study, the complexes did not show any weak band around 847-803 cm^{-1} [1], which also indicated the absence of coordinated water molecule.

Table 1. Analytical and physical data of the ligands and complexes

Ligand / Complex (No.)	M. P. (ºC)	Colour	Yield (%)	Elemental analyses Cal. (Found)			μ_{eff} (B.M.)	Λ_M (Ω^{-1} cm^2 mol^{-1})
				C	H	M		
Cyanex 301 (L)								
$[ZnL_2]$ (**1**)	250	White	65	54.30(54.20)	09.16(09.12)	09.23(09.20)	Dia. [c]	04.03
$[CdL_2].H_2O$ (**2**)	244	White	40	49.67(49.52)	08.80(08.88)	14.54(14.49)	Dia. [c]	07.05
$[HgL_2].H_2O$ (**3**)	262	White	43	39.47(39.38)	06.98(07.00)	20.60(20.58)	Dia. [c]	06.20
Cyanex 302 (L´)								
$[ZnL´_2]$ (**4**)	279	White	58	56.58(56.70)	10.14(10.10)	09.67(09.60)	Dia. [c]	05
$[CdL´_2].H_2O$ (**5**)	258	White	49	51.62(51.79)	09.25(09.19)	15.17(15.11)	Dia. [c]	09
$[HgL´_2].H_2O$ (**6**)	247	White	52	46.11(46.20)	08.26(08.20)	24.19(24.10)	Dia. [c]	09

[c] Diamagnetic

Table 2. The most important bands in the IR spectra of the ligands and complexes

Ligand / Complex (No.)	ν (O-H)[d]	ν (O-H)[e]	ν (S-H)	ν (P=S)	ν (M-S)	ν (M-O)
Cyanex 301 (L)			2638 m	637 m	-	
[ZnL_2] (**1**)				589 m	408 w	
[CdL_2].H_2O (**2**)	3370 b			590 m	407 w	
[HgL_2].H_2O (**3**)	3439 b			586 m	411 w	
Cyanex 302 (L´)		2343 s		634 m	-	
[$ZnL´_2$] (**4**)				587 m	418 w	507 w
[$CdL´_2$].H_2O (**5**)	3440 b			575 m	410 w	512 w
[$HgL´_2$].H_2O (**6**)	3425 b			581 m	408 w	506 w

[d] Water

[e] Include P-OH

where, b = broad, s= strong, m = medium and w = weak

3.3. Electronic spectra and magnetic measurements

The electronic spectra of Zn (II), Cd (II) and Hg (II) complexes showed no bands due to d-d transition. This phenomenon is natural as there is no possibility of transition due to non availability of empty *d*-orbital [13]. Besides, all complexes showed no appreciable absorbtions in the region above 400 nm, in accord with the d^{10} electronic configuration of the Zn (II), Cd (II) and Hg (II) ions [12, 14, 15]. The complexes are diamagnetic due to non availability of unpaired electrons [13]. A tetrahedral geometry was suggested for the Zn (II), Cd (II) and Hg (II) complexes.

Table 3. Antibacterial activity of the ligands and complexes

Ligand /Complex (No.)	Antibacterial activity (zone of inhibition in mm)		
	E. coli (40 µg/disc)	*S. aureus* (40 µg/disc)	*S. typhi* (40 µg/disc)
Cyanex 301 (L)	07	00	08
[ZnL_2] (**1**)	18	16	10
[CdL_2].H_2O (**2**)	11	10	00
[HgL_2].H_2O (**3**)	15	19	00
Cyanex 302 (L´)	07	00	00
[$ZnL´_2$] (**4**)	16	15	09
[$CdL´_2$].H_2O (**5**)	10	13	00
[$HgL´_2$].H_2O (**6**)	14	16	00
Ciprofloxacin	24	22	22
DMSO (Control)	00	00	00

3.4. Antimicrobial studies

The biological activities of the ligands and their metal complexes were determined at a concentration of 40 µg/disc against three pathogenic bacteria and three pathogenic fungi. The standard drugs ciprofloxacin and griseofulvin were also tested for their antibacterial and antifungal activities at the same concentration under the conditions similar to that of the test compounds. The results of biological activities tested for the free ligands and their complexes are given in Table 3 and 4. The diameter of inhibition zone (mm) including the disc diameter was measured for each treatment. The ligands presented no activity against the all tested microorganisms under identical experimental conditions. The antibacterial activity results revealed that the complex **1** showed maximum activity with the zone of inhibition 18 mm, while the complexes **3**, **4** and **6** exhibited moderate activity with the zone of inhibition 14-16 mm against *E. coli* as compared to standard drug. The complex **3** exhibited almost similar activity with the zone of 19 mm, but the complexes 1, 4 and 6 displayed very good activity with the zone of 15-16 mm against *S. aureus* when compared to the standard drug. Besides, the antifungal activity results revealed that the complexes **1, 2, 4** and **6** showed moderate activity with the zone of inhibition 14-17 mm against *A. niger* as compared to standard drug. The complexes **2**, **3** and **4-6** exhibited moderate activity with the zone of 13-15 mm against *F. oxysp.* when compared to the standard drug and the complex **4** displayed highest activity with the zone of 20 mm against *Tricho. sp.* as compared to standard drug.

Further, a comparative study of the ligands and their metal complexes also indicated that the metal chelates exhibited higher antimicrobial activities than the free ligands. Such increased antimicrobial activity of the metal chelates can be explained on the basis of chelation theory. On chelation, the polarity of the metal ion will be reduced to a greater extent due to the overlap of the ligand orbital and partial sharing of the positive charge of the metal ion with donor groups [16].

Table 4. Antifungal activity of the ligands and complexes

Ligand /Complex (No.)	Antifungal activity (zone of inhibition in mm)		
	A. niger (40 μg/disc)	*F. oxysp.* (40 μg/disc)	*Tricho. sp.* (40 μg/disc)
Cyanex 301 (L)	00	07	00
[ZnL´$_2$] (**1**)	14	10	00
[CdL´$_2$].H_2O (**2**)	14	15	00
[HgL´$_2$].H_2O (**3**)	10	13	00
Cyanex 302 (L´)	00	00	07
[ZnL´$_2$] (**4**)	17	13	20
[CdL´$_2$].H_2O (**5**)	11	15	08
[HgL´$_2$].H_2O (**6**)	16	13	00
Griseofulvin	24	23	26
DMSO (Control)	00	00	00

References

[1] Revanasiddappa, M.; Suresh, T.; Khasim, S.; Raghavendra, S. C.; Basavaraja, C.; Angadi, S. D., *J. Chem.,* **5**, 395-403, 2008.

[2] Islam, M. S.; Talukder, M. K. H., *J. Bang. Sci. Chem. Soc.,* **8**, 105-110, 1995.

[3] Islam, M. B.; Haque, M. Z.; Islam, M. S., *Ban. J. Sci. Ind. Res.,* **42**, 475-482, 2007.

[4] Beur, A. W.; Kirby, W.M.M.; Sherris, J.C.; Turck, M., *Am. J. Clin. Pathol*, **44**, 493-496, 1966.

[5] Rios, J.J.; Reico, M.C.; Villar, A., *J. Entho. Pharmacol*. **23**, 127-149, 1988.

[6] El-Tabl, A.S.; El-Saied, F.A.; Plass, W.; Al-Hakimi, A.N., *Spectrochim. Acta Mol. Biomol. Spectrosc.,* **71**, 90-99, 2008.

[7] Rockett, J., *App. Spectrose.* **16**, 39-40, 1962.

[8] Shagidullin, R.R.; Lpatova, I.P., *Russian Chem. Bul.* **20**, 940-942, 1971.

[9] Leka, Z.; Grujic, S.A.; Tesic, Z.; Lukic, S.; Skuban, S.; Trifunovic, S., *J. Serb. Chem. Soc.,* **69**, 137-143, 2004.

[10] Silverstein, R.M.; Bassler, G.C.; Morrill, T.C., Spectrometric identification of organic compounds, John Wiley and sons, Singapore, p. 170.

[11] Swamy S. J.; Reddy E. R.; Raju D.; Jyothi N. S., *Molecules*, **11**, 1000-1008, 2006.

[12] Naik, A.D.; Revankar, V.K.; *Proc. India Acad. Sci. (Chem. Sci.)*, **113**, 285-290, 2001.

[13] Desai, R.M.; Shah, M.K.; Shah, V.H., *J. Chem.*, **3**, 137-141, 2006.

[14] Saghatforoush, L.A.; Aminkhani, A.; Ershad, S.; Karimnezhad, G..; Ghammamy, S.; Kabiri, R., *Molecules*, **13**, 804-811, 2008.

[15] Majumder, A.; Rosair, G. M.; Mallick, A.; Chattopadhyay, N.; Mitra, S., *Polyhedron*, **25**, 1753-1762, 2006.

[16] Raman, N.; Raja, J.D.; Sakthivel, A., *J. Chem. Sci.*, **119**, 303-310, 2007.

Order and Type of Entire Functions Represented by Multiple Dirichlet Series in Several Complex Variables

Md. Feruj Alam[1] and Dr. Md. Muklesur Rahman[2]
[1]Department of Mathematics, Rajshshi University of Engineering & Technology (RUET), Rajshahi-6204.
[2]Department of Mathematics, University of Dhaka, Dhaka -1000.
E-mail: ferujalam@yahoo.com

Abstract

The entire functions are represented by multiple Dirichlet series in several complex variables having the same sequence of exponents. The nature of Gol'dberg order and Gol'dberg type has been studied.

1. Notations

The *n*-tuples $(\sigma_1,\cdots,\sigma_n),(m_1,\cdots,m_n)$, $(s_1,\cdots,s_n)$ of C^n or R^n (complex *n*-space or real *n*-space) will be respectively denoted by their corresponding unsuffixed symbol σ, m, s. By I^n, it will mean the Cartesian product of *n* copies of *I* where, *I* is the set of non-negative integers. For $s, w \in C^n$ and $\alpha \in C$ where, it is defined as

(*i*) $s+w=(s_1+w_1,\cdots,s_n+w_n)$ (*ii*) $\alpha s=(\alpha s_1,\cdots,\alpha s_n)$

(*iii*) $s.w=s_1w_1+\cdots+s_nw_n$

For $a \in R$, $s \in C^n$

(*iv*) $s+a=(s_1+a,\cdots,s_n+a)$

The positive hyperoctant R_+^n in R^n will be denoted by

$$R_+^n=\{x : x \in R^n, \quad x_i \geq 0,\ j=1,\cdots,n\}$$

For $t \in R_+^n$, we set $\|t\|=t_1+\cdots+t_n$.

For $k \in R$, $\bar{k}$ will denote the real *n*-tuple $(k,\cdots,k)$. For an entire function, *f* with domain C^n, f^k will denote the function $\dfrac{\partial^{\|k\|}f}{\partial^{k_1}s_1\cdots\partial^{k_n}s_n}$, where $k \in I^n$ and $f^{(\bar{0})}=f$.

It is denoted the *n*-tuple $(\lambda_{1m_1},\cdots,\lambda_{nm_n})$ by $\lambda_{n,m}$

Thus, $s.\lambda_{n,m}=s_1\lambda_{1m_1}+\cdots+s_n\lambda_{nm_n}$

2. Introduction

The multiple Dirichlet series is considered as

$$f(s_1,\cdots,s_n)=\sum_{m_1,\cdots,m_n=1}^{\infty}a_{m_1\cdots m_n}\exp\{s_1\lambda_{1m_1}+\cdots+s_n\lambda_{nm_n}\},$$

or,

$$f(s)=\sum_{m=1}^{\infty}a_m\exp\{s.\lambda_{n,m}\}, \tag{1}$$

$(s_j=\sigma_j+i\tau_j\in C,\ \text{j}=1,\cdots,\text{n}),\ a_m\in C$, and $\{\lambda_{jm_j}\}_{m_j=1}^{\infty},\ j=1,\cdots,n.$ are n sequences of exponents satisfying the conditions

$$0<\lambda_{j1}<\lambda_{j2}<\cdots<\lambda_{jk}\to\infty \text{ as } k\to\infty, \quad \text{for } j=1,\cdots,n. \tag{2}$$

Throughout it is assume that

$$\lim_{m_j\to\infty}\frac{\log m_j}{\lambda_j m_j}=0, \quad j=1,\cdots,n \ldots\ldots \tag{3}$$

If (3) holds then the domain of convergence of the series (1) coincides with its domain of absolute convergence [1].

All the multiple Dirichlet series of the form (1) having the same sequence of exponents $\{\lambda_{jm_j}\}_{m_j=1}^{\infty}\ j=1,\cdots,n,$ satisfying (2) which are absolutely and uniformly convergent in C^n and hence are entire functions.

Let $f(s)=\sum_{m=1}^{\infty}a_m\exp\{s.\lambda_{n,m}\}$ and $g(s)=\sum_{m=1}^{\infty}b_m\exp\{s.\lambda_{n.m}\}$ (4)

For $k\in I^n$, we define

$$f^k(s)=\sum_{m=1}^{\infty}\lambda_{n,m}^k a_m\exp\{s.\lambda_{n,m}\} \text{ and } g^k(s)=\sum_{m=1}^{\infty}\lambda_{n,m}^k b_m\exp\{s.\lambda_{n.m}\} \tag{5}$$

3. Definitions

It is defined the poly half plane D_l as $D_l=\{S:S\in C^n,\ \text{Re}\,s=\sigma<<l\}$, where $l\in R^n$. Such domains are called fundamental domains. Then the region D_l+r, depending on the parameter $r\in R$, is defined as $D_l+r=\{s+r,s\in D_l\}$. Then for the entire function *f*, given by (1) , it is defined the maximum modulus $M_{f,D_l}(r)$ with respect to the region D_l, where $r\in R$ as $M_{f,D_l}(r)=\sup\{|f(s):s\in D_l+r\}$.

Let $f\in F$ and D_l be a fundamental domain. Also, let S_f be the set of points $\alpha\in R$ such that for every $\alpha\in S_f$, there corresponding an $r_0\in R$ such that

$\log M_{f,D_l}(r)\le e^{r\alpha}$, for $r\ge r_0$.

The infimum of the set S_f is called the Gol'dberg order $\rho(D_l)$ of f with respect to the region D_l. It is says that f is of infinite or finite Gol'dberg order according as S_f is empty or non-empty.

Next, for the Gol'dberg order $\rho(D_l)>0$, let $K_f(\rho)$ be the set of all $K\in R$ such that

$\log M_{f,D_l}(r) \le Ke^{r\alpha}$, for $r \ge r_0$.

The infimum of the set $K_f(\rho)$ is called the Gol'dberg type $T(D_l)$ of f corresponding to $\rho(D_l)$. As before, it is says that f is of infinite or finite Gol'dberg type according as $K_f(\rho)$ is empty or non-empty.

Now, Gol'dberg order and Gol'dberg type simply written as *G*-order and *G*-type respectively. From the definition it follows easily that

$$\rho(D_l) = \limsup_{r\to\infty} \frac{\log\log M_{f,D_l}(r)}{r} \tag{6}$$

$$\rho_k(D_l) = \limsup_{r\to\infty} \frac{\log\log M_{f^k,D_l}(r)}{r} \tag{7}$$

$$T(D_l) = \limsup_{r\to\infty} \frac{\log M_{f,D_l}(r)}{e^{r\rho(D_l)}}, \quad \text{if } \rho(D_l) > 0 \tag{8}$$

$$T_k(D_l) = \limsup_{r\to\infty} \frac{\log M_{f^k,D_l}(r)}{e^{r\rho_k(D_l)}}, \quad \text{if } \rho_k(D_l) > 0 \tag{9}$$

It is known that the *G*-order $\rho(D_l)$ does not dependent on the choice of the domain D_l while *G*-type $T(D_l)$ does [2]. Hence it may be written ρ instead of $\rho(D_l)$. It is also known [2] that

$$\rho = \limsup_{m\to\infty} \frac{\lambda_{n,m}\log\lambda_{n,m}}{-\log|a_m|} \tag{10}$$

$$\rho_k = \limsup_{m\to\infty} \frac{\|\lambda_{n,m}\|\log\|\lambda_{n,m}\|}{-\log|a_m\lambda_{n,m}^k|} \tag{11}$$

$$T(D_l) = \frac{1}{e\rho}\limsup_{m\to\infty}\left[\lambda_{n,m}\left\{|a_m|\varphi_{D_l}(m)\right\}^{\frac{\rho}{\lambda_{n,m}}}\right] \tag{12}$$

where $\varphi_{D_l}(m) = \sup_{S\in D_l}|\exp\{s.\lambda_{n,m}\}$

$$T_k(D_l) = \frac{1}{e\rho}\limsup_{m\to\infty}\left[\|\lambda_{n,m}\|\left\{|\lambda_{n,m}^k a_m|\varphi_{D_l}(m)\right\}^{\frac{\rho}{\|\lambda_{n,m}\|}}\right] \tag{13}$$

Theorem 1: If $f(s)$ and $g(s)$ given by (4) be two entire functions of *G*-order $\rho(f)$ and $\rho(g)$ respectively and if $\rho(g) > \rho(f)$ then the *G*-order of $f^k(s) + g^k(s)$ is equal to $\rho_k(g)$.

Proof: Since $f(s)$ and $g(s)$ are entire functions, $f^k(s)$ and $g^k(s)$ given by (5) are entire functions and so $f^k(s)+g^k(s)$ is also entire functions. Let $\rho_k(f)$ and $\rho_k(g)$ are respectively the *G*-order of $f^k(s)$ and g^k. Let $\rho_k(f+g)$ be the G-order of $f^k(s)+g^k(s)$, then by (7),

$$\rho_k(f) = \limsup_{r\to\infty} \frac{\log\log M_{f^k,D_l}(r)}{r}$$

$$\rho_k(g) = \limsup_{r\to\infty} \frac{\log\log M_{g^k,D_l}(r)}{r}$$

$$\rho_k(f+g) = \limsup_{r\to\infty} \frac{\log\log M_{f^k+g^k,D_l}(r)}{r}$$

Now,

$$M_{f^k+g^k,D_l}(r) = \sup_{s\in D_l+r} |f^k(s)+g^k(s)|$$

$$\leq \sup_{s\in D_l+r} |f^k(s)| + \sup_{s\in D_l+r} |g^k(s)|$$

$$\leq M_{f^k,D_l}(r) + M_{g^k,D_l}(r)$$

$$\leq \exp\left\{e^{r(\rho_k(f)+\varepsilon)}\right\} + \exp\left\{e^{r(\rho_k(g)+\varepsilon)}\right\},\ \varepsilon>0$$

$$< 2\exp\left\{e^{r(\rho_k(g)+\varepsilon)}\right\} \quad \text{for } r > r_0(\varepsilon)$$

Hence,

$$\limsup_{r\to\infty} \frac{\log\log M_{f^k+g^k,D_l}(r)}{r} < \rho_k(g)+\varepsilon$$

Thus

$$\rho_k(f+g) \leq \rho_k(g). \tag{14}$$

On the other hand, there exists n-sequences of values of $r^{(m)}\to\infty$ as $m\to\infty$ such that

$$M_{g^k,D_l}(r^{(m)}) > \exp\left\{e^{r^{(m)}(\rho_k(g)-\varepsilon)}\right\},\quad m\in I,\ r\in R.$$

Again,

$$M_{f^k+g^k,D_l}(r^{(m)}) \geq \exp\left\{e^{r^{(m)}(\rho_k(g)-\varepsilon)}\right\} - \exp\left\{e^{r^{(m)}(\rho_k(f)+\varepsilon)}\right\}$$

$$= \exp\left\{e^{r^{(m)}(\rho_k(g)-\varepsilon)}\right\}\left[1-\frac{\exp\{e^{r^{(m)}(\rho_k(f)+\varepsilon)}\}}{\exp\{e^{r^{(m)}(\rho_k(g)-\varepsilon)}\}}\right]$$

$$> \frac{1}{2}\exp\left\{e^{r^{(m)}(\rho_k(g)-\varepsilon)}\right\}$$

provided, ε > 0 is so small that $\rho_k(f)+\varepsilon < \rho_k(g)-\varepsilon$ and m is sufficiently large.

Thus,

$$\rho_k(f+g) \geq \rho_k(g) \tag{15}$$

Combining (14) and (15), we have,

$$\rho_k(f+g) = \rho_k(g)$$

Hence the theorem is proved.

Theorem 2: If $f(s) = \sum_{m=1}^{\infty} a_m \exp\{s.\lambda_{n,m}\}$ and $g(s) = \sum_{m=1}^{\infty} b_m \exp\{s.\lambda_{n,m}\}$ be two entire function of *G*-order $\rho(f)\,(0 < \rho(f) < \infty)$ and $\rho(g)\,(0 < \rho(g) < \infty)$ respectively and if $\rho(g) \geq \rho(f)$ then the *G*-order $\rho_k(fg)$ of $f^k g^k \leq \max[\rho_k(f), \rho_k(g)]$.

Proof: Since $f^k(s)$ and $g^k(s)$ are entire functions of *G*-order $\rho_k(f)(0 < \rho_k(f) < \infty)$ and $\rho_k(g)(0 < \rho_k(g) < \infty)$ respectively, we have,

$$M_{f^k,D_l}(r) < \exp\{e^{r(\rho_k(f)+\varepsilon)}\} \quad \text{and}$$

$$M_{g^k,D_l}(r) < \exp\{e^{r(\rho_k(g)+\varepsilon)}\}$$

for ε > 0 and sufficiently large $r > r_0(\varepsilon)$.

Now, $M_{f^k g^k,D_l}(r) = \sup_{s \in D_l + r} |f^k(s)g^k(s)| \leq M_{f^k,D_l}(r) M_{g^k,D_l}(r)$

$$\leq \exp\{e^{r(\rho_k(f)+\varepsilon)}\} \exp\{e^{r(\rho_k(g)+\varepsilon)}\}$$

$$\leq \exp\{2e^{r(\rho_k(g)+\varepsilon)}\}.$$

Hence, $\rho_k(fg) \leq \rho_k(g)$.

Then it follows that $\rho_k(fg) \leq \max[\rho_k(f), \rho_k(g)]$.

Theorem 3: Let $f(s)$ and $g(s)$, given by (4) be two entire functions of the same *G*-order $\rho\ (0 < \rho < \infty)$. Let $T_{D_l}(f)$ and $T_{D_l}(g)$ be their respective *G*-type with respective to the fundamental domain D_l. Then $f^k + g^k$ will be of *G*-order ρ_k and *G*-type $T_{k,D_l}(f+g)$ such that $T_{k,D_l}(f+g) = \max[T_{k,D_l}(f), T_{k,D_l}(g)]$.

Proof: Let $T_{k,D_l}(f)$ and $T_{k,D_l}(g)$ be the *G*-type with respect to fundamental domain D_l of

$f^k(s) = \sum_{m=1}^{\infty} \lambda_{n,m}^k a_m \exp\{s.\lambda_{n,m}\}$ and $g^k(s) = \sum_{m=1}^{\infty} \lambda_{n,m}^k b_m \exp\{s.\lambda_{n,m}\}$ respectively.

Let us suppose that $T_{k,D_l}(f) > T_{k,D_l}(g)$. Then by (9)

$$T_{k,D}(f) = \lim_{r\to\infty} \sup \frac{\log M_{f^k,D}(r)}{e^{r\rho_k}}, \quad \text{and}$$

$$T_{k,D_l}(g) = \lim_{r\to\infty} \sup \frac{\log M_{g^k,D_l}(r)}{e^{r\rho_k}},$$

Now by definition,

$$M_{f^k,D_l}(r) < \exp\{(T_{k,D_l}(f)+\varepsilon)e^{r\rho_k}\} \quad \text{and}$$

$$M_{g^k,D}(r) < \exp\{(T_{k,D}(g)+\varepsilon)e^{r\rho_k}\} \quad \text{for } \varepsilon > 0 \text{ and } r > r'$$

Again,

$$M_{f^k+g^k,D}(r) \leq M_{f^k,D}(r) + M_{g^k,D}(r)$$

$$\leq \exp\{(T_{k,D}(f)+\varepsilon)e^{r\rho_k}\}+\exp\{(T_{k,D}(g)+\varepsilon)e^{r\rho_k}\}$$
$$\leq 2\exp\{(T_{k,D_l}(f)+\varepsilon)e^{r\rho_k}\}, \text{ and so.}$$
$$T_{k,D_l}(f+g) \leq T_{k,D_l}(f) \tag{16}$$

Also,

$$M_{f^k+g^k,D_l}(r) \geq \exp\{(T_{k,D_l}(f)-\varepsilon)e^{r\rho_k}\}-\exp\{(T_{k,D_l}(g)+\varepsilon)e^{r\rho_k}\}$$
$$> \frac{1}{2}\exp\{(T_{k,D_l}(f)-\varepsilon)e^{r\rho_k}\}$$

Provided $\varepsilon > 0$ is so small that $T_{k,D_l}(g)+\varepsilon < T_{k,D_l}(f)-\varepsilon$, and so,

$$T_{k,D_l}(f+g) \geq T_{k,D_l}(f) \tag{17}$$

Combining (16) and (17), we have,

$$T_{k,D_l}(f+g) = T_{k,D_l}(f)$$

Similarly it can be easily show that $T_{k,D_l}(f+g) = T_{k,D_l}(g)$

Hence

$$T_{k,D_l}(f+g) = \max\left[T_{k,D_l}(f), T_{k,D_l}(g)\right]$$

References

[1] Janusauskas, A.I., "Elementary theorems on the convergence of double Dirichlet series" Soviet Math. Doki. Vol. 18 no. 3, pp 610 – 614, 1977.

[2] Sarker. P.K., "On Gol'dberg order and Gol'dberg type of an entire function of several complex variables represented by multiple Dirichlet series." Indian J. of pure and App. Math. 13(10), pp 1221- 1229, 1982.

Phase Conjugation as a Dispersion Compensator of Fiber Optic Cables

M. S. Hossain*, M.A.G. Khan, S. C. Majumder, M. I. Hossain
Department of Electrical and Electronic Engineering
Rajshahi University of Engineering & Technology, Rajshahi-6204, Bangladesh.
*E-mail: selim_hossain@yahoo.com

Abstract

This paper presents Phase Conjugation to Dispersion Compensation of Dispersion Control Characteristics of the Fiber Optic Cables. Phase conjugation is a fascinating phenomenon with very unusual characteristics and properties. The effective compensation of waveform distortion due to chromatic dispersion in a single-mode fiber was demonstrated using an optical phase-conjugate (OPC) wave generated by no degenerate forward four-wave mixing in a zero-dispersion single-mode fiber. After transmission of 5-Gb/s and 6-Gb/s continuous-phase FSK (CPFSK) signal through a dispersive single-mode fiber, distortion compensation was confirmed by measuring bit error rate characteristics and observing heterodyne-detected eye-patterns. The performances of the proposed Phase Conjugation method are investigated and compared to those obtained from the Fiber Bragg Grating (FBG) at various operating conditions, such as, Eye diagram at transmitting, receiving and corresponding histogram, etc. The comparative results show that the Phase conjugation is more reliable and hence, found to be a suitable replacement of the Fiber Bragg Grating (FBG) technique.

Key words: Phase Conjugator, Fiber Bragg Grating, LASERs & LEDs, OptoSim software, Dispersion Compensation, Eye Diagram, SI Fiber and GRIN fiber.

1. Introduction

The dispersion of optical components is an important parameter, which has a significant effect on the performance of various optical systems. Analysis and accurate measurement of the dispersion is therefore essential in optimization of the performance of such systems. Measurements of chromatic dispersion can be performed by applying various techniques. The dispersion of an optical fiber has been an important characteristic to be measured. In practice, it is important to have knowledge of such parameters as the zero-dispersion wavelength, the dispersion slope and uniformity of the dispersion of the manufactured fiber. The dispersion of optical components as optical filters has gained a lot of interest. The development of the filters based on fiber Bragg gratings (FBGs) permit for compensation of the dispersion of an optical fiber. By applying FBGs, the dispersion effects can be dramatically decreased in long-transmission systems [2].The FBG techniques has some problems, it requires more number of occurrences and BER is not satisfactory. This concept of waves colliding and rebounding provides the key insight into understanding the otherwise mysterious phenomenon of phase conjugation. When different wavelength of light pulses are launched into an optical fiber these pulse will traveled at different speeds due to the variation refractive index with wavelength [9]. The schematic setup for dispersion by phase conjugation shows in Figure 3. The block diagram consists of primary link, phase conjugator and secondary link for dispersion control. With the increasing of the bit rate, high efficient and broadband OPC is needed for the next generation of high speed all optical network. Also increases both the data & length of the fiber compared to Fiber Bragg grating technique [1, 4].

2. Phase Conjugate Mirror

Let us begin with the properties of a phase conjugate mirror. A phase conjugate mirror is like a mirror, in that it reflects incident light back towards where it came from, but it does so in a different way than a regular mirror [10]. In a regular mirror, light that strikes the mirror normal to its surface, is reflected straight backing the way it came (A). This is also true of a phase conjugate mirror (B). When the light strikes a normal mirror at an angle, it reflects back in the opposite direction, such that the angle of incidence is equal to the angle of reflection (C). In a phase conjugate mirror, on the other hand, light is always reflected straight back the way it came from, no matter what the angle of incidence (D) as shown in Figure 1.

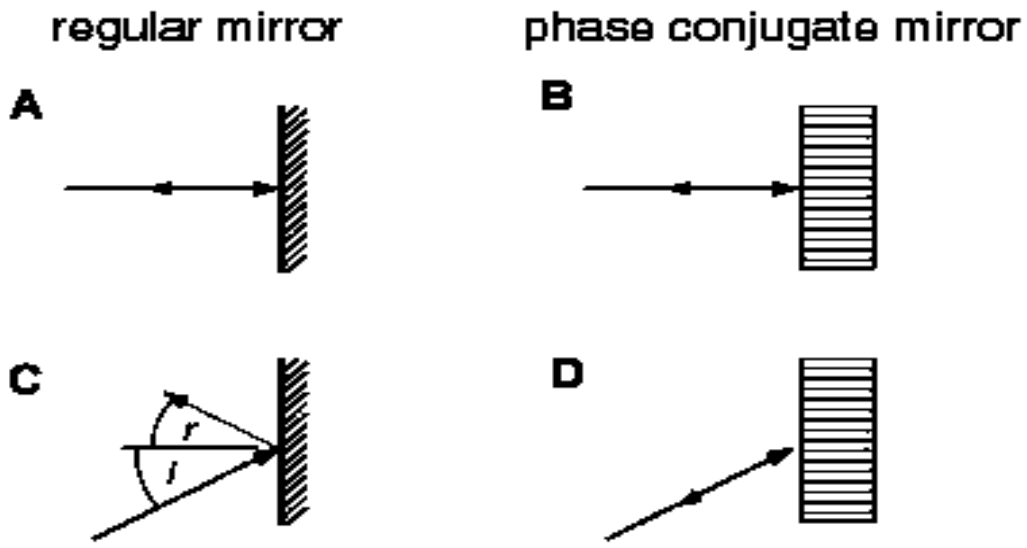

Figure 1. Phase Conjugate Mirror & Regular Mirror

3. LASERs and LEDs

Models are provided for continuous wave (CW) lasers and mode-locked lasers to be used in conjunction with external modulators, as well as direct modulated semiconductor lasers [1,5]. The rate equations are used to produce accurate optical waveform results. The AM response, FM response, relative intensity noise, self-phase modulation, cavity dispersion, timing jitter, L-I curve, and small signal frequency responses are all included. A rate-equation-based LED model includes important behavioral aspects such as electrical parasitic, optical line width, and relative intensity noise (RIN). The Best Fit Laser Toolkit enables rate equation laser parameters to be easily configured by entering in manufacturer data sheet information or actual measurements of specific lasers. An Electrical Circuit Model Generator™ enables the rate equation laser model to be output to an electrical circuit for simulation in electrical circuit simulation tools such as SPICE. This unique capability provides the ability to simulate both the laser driver and semiconductor laser together for the most accurate consideration of parasitic coupling and driving conditions in the simulation Figure 2 show the Optical spectrum from LASER Diode. The most common and practical type of laser diode is formed from a p-n junction and powered by injected electrical current [1,3,5,11]. Many types of laser diodes known today collectively form a subset of the larger classification of semiconductor p-n junction diodes [6].

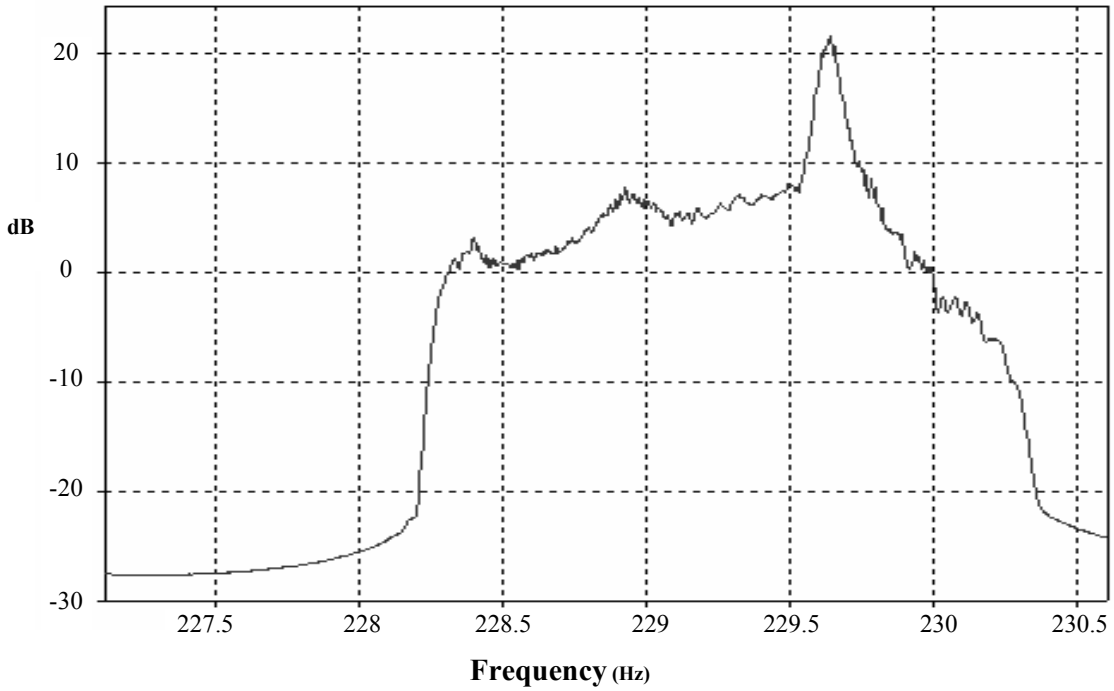

Figure 2. Optical spectrum from LASER Diode.

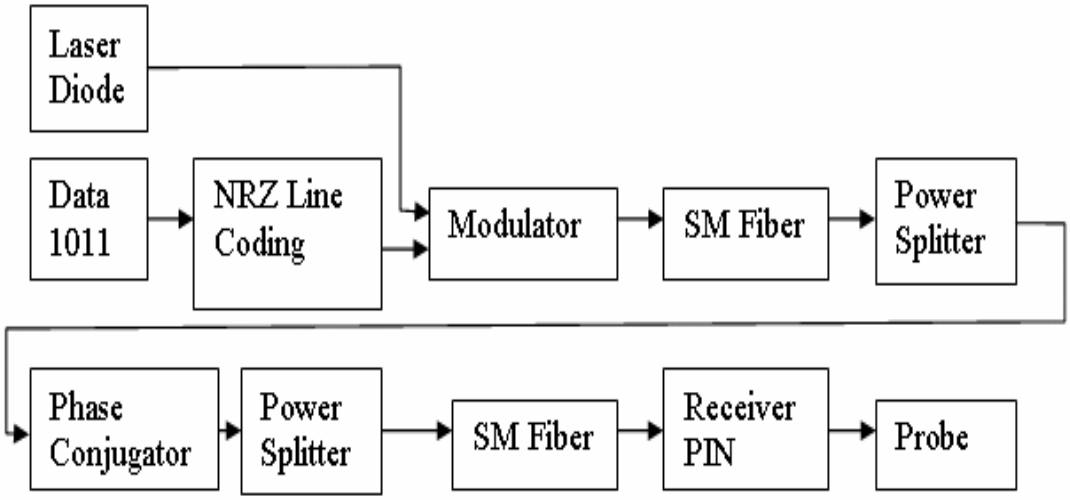

Figure 3. Schematic setup for dispersion by phase conjugation

4. Governing Equations for Dispersion Compensation

Refractive indexes vary with wavelength. So light velocity through fiber will be changed with change of wavelength spectral width which limits the information capacity of a fiber optic channel [1,4].

Group velocity, $v_g = \frac{d\omega}{d\kappa}$ where $\omega = 2\pi f$, $\kappa = \frac{2\pi}{\lambda}$

$$v_g = \frac{d\omega}{d(\frac{2\pi}{\lambda})} = \frac{df}{d(\frac{1}{\lambda})} = -\lambda^2 \frac{df}{d\lambda} \quad \ldots\ldots\ldots\ldots\ldots\ldots (1)$$

Phase velocity, $v_p = f\lambda \Rightarrow \frac{c}{n} = f\lambda \Rightarrow f = \frac{c}{n\lambda}$ …(2)

Now, $v_g = -c\lambda^2 \frac{d}{d\lambda}(\frac{1}{n\lambda}) = \frac{c}{n}(1 + \frac{\lambda}{n}\frac{dn}{d\lambda})$ ……..(3)

we get, $\Delta v_g = \frac{dv_g}{d\lambda}\Delta\lambda$ ……(4)

$$= \frac{c\lambda}{n^2}[\frac{d^2n}{d\lambda^2} - \frac{2}{n}(\frac{dn}{d\lambda})^2]\Delta\lambda \quad \ldots\ldots.. (5)$$

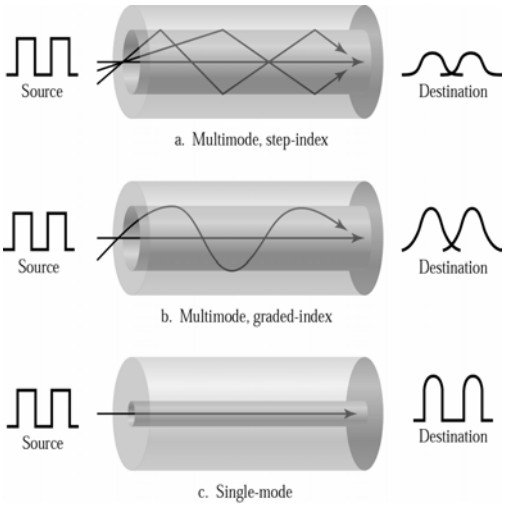

Figure 4. Mode related dispersion

Material dispersion. $M = -\frac{\lambda}{c}\frac{d\eta^2}{d\lambda^2}$. The unit of *M* is $ps/(nm \cdot km)$ For silica fiber is given by an empirical formula, $M = -\frac{M_0\lambda}{4}\left(1 - \frac{\lambda_0^4}{\lambda^4}\right)$ ……..(6)

Where the slope M_0 is approximately -0.095 $ps/(nm \cdot km)$, λ_0 is the zero dispersion wavelength which is about 1310 nm, and wavelengths are in nm. A Matlab plot of this equation is shown below:

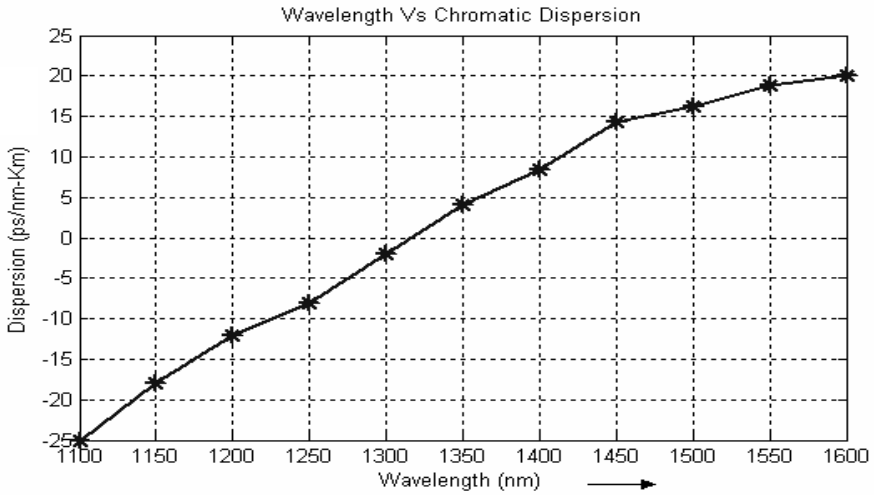

Figure 5. Chromatic dispersion with respect to wavelength

5 Modal Distortion

When different wavelength of light pulses are launched into an optical fiber these pulse will traveled at different speeds due to the variation refractive index with wavelength. These light waves tend to get spread out in time after traveling some distance in the fiber and this is continued through out the length of the fiber. This phenomenon of boarding the pulse width is called dispersion practically as the light sources are neither monochromatic nor coherent. So the light sources must have some spectral width. That is there are several wavelengths around a central wavelength. The dispersion of optical components is an important parameter, which has a significant effect on the performance of various optical systems. Analysis and accurate measurement of the dispersion is therefore essential in optimization of the performance of such systems [13].

Measurements of chromatic dispersion can be performed by applying various techniques. By using Equation (1-6), we can easily calculate and plot the chromatic dispersion with respect to wavelength which shown in Figure 5.

6. Simulation Results and Discussion

OptoSim Software includes a wide range of tools for performing simulation results analysis, plotting, and post-processing of simulation results. Signal waveforms, eye diagrams, frequency chirp, signal spectra, dispersion and power maps, autocorrelation plots, constellation and scattering diagrams, and other results may be viewed at any point in the system topology using predefined plot or interactive analysis options. Interactive plot tools can be used to change the type and format of a plot produced at any point in the system without re-running the simulation, as well as provide post-processing functionality (e.g. graph superimposition, correlation graphs, interactive cursor read-out data, peak search, eye-diagram measures, BER that allows the user to simulate the project and perform further analysis of results at a later time (saving time during design process). The Various simulation result curves shown in Figure (6-9) for Fiber Bragg Grating and Phase conjugation. From the optical probes before and after the OPC shown in Figure 6 & 7, it can be seen that the phase conjugator near the center of the span reverses the broadening (spectral Inversion) and that this allows the broadening to be zero at the receiver and the pulse shape is restored to its input form. Figure 7 (a) and (b) show Eye diagram of the received signals using Fiber Bragg Grating (FBG) and Phase Conjugation methods. It is found from this figure, Phase Conjugation methods gives less BER. Figure 9(a) and (b) show the Corresponding histogram of electrical samples of FBG and OPC.

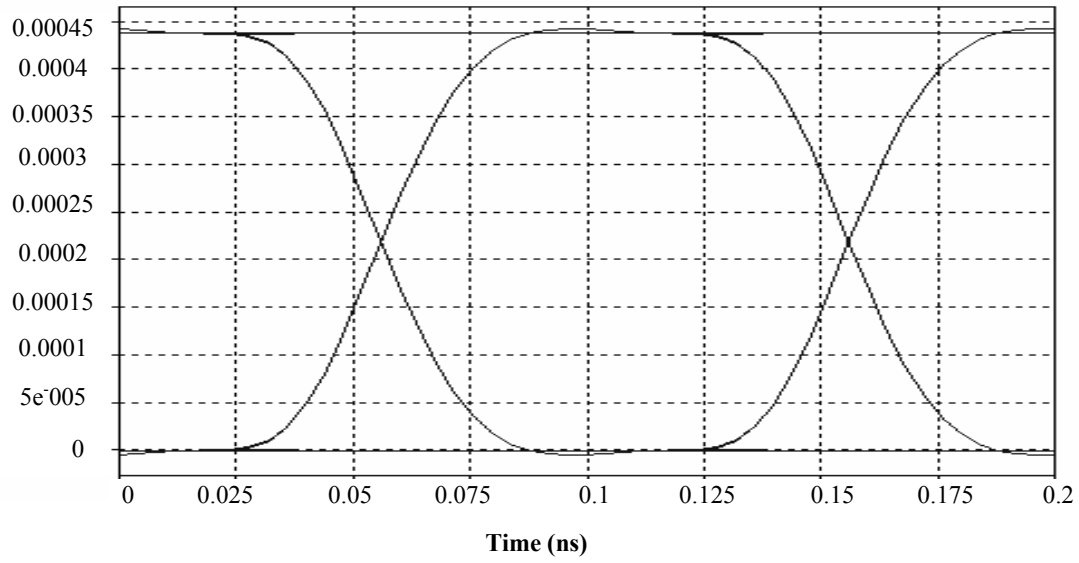

Figure 6. Simulated eye diagram at transmitting side

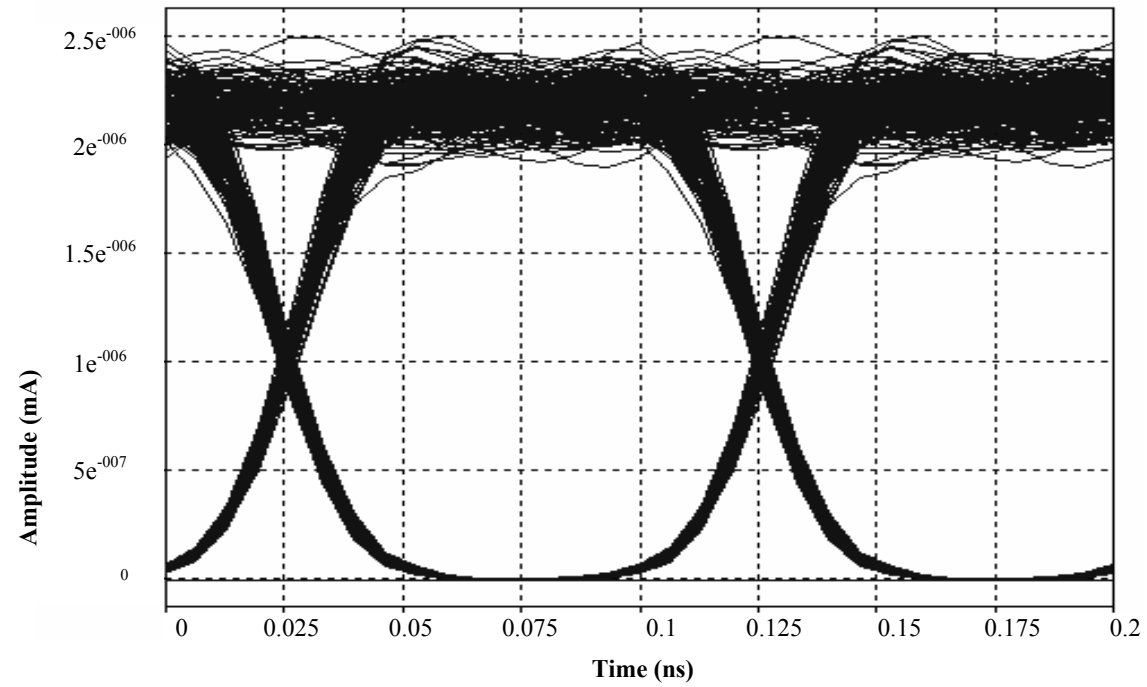

(a)

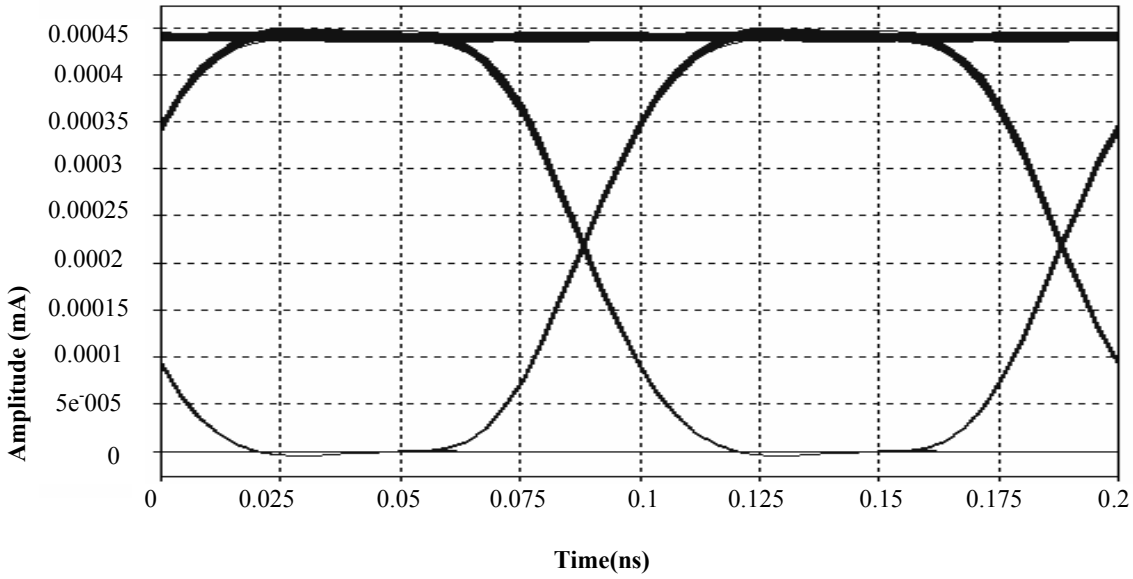

(b)

Figure 7. Simulated eye diagram using (a) Fiber Bragg grating & (b) Phase conjugation at receiving end (larger opening)

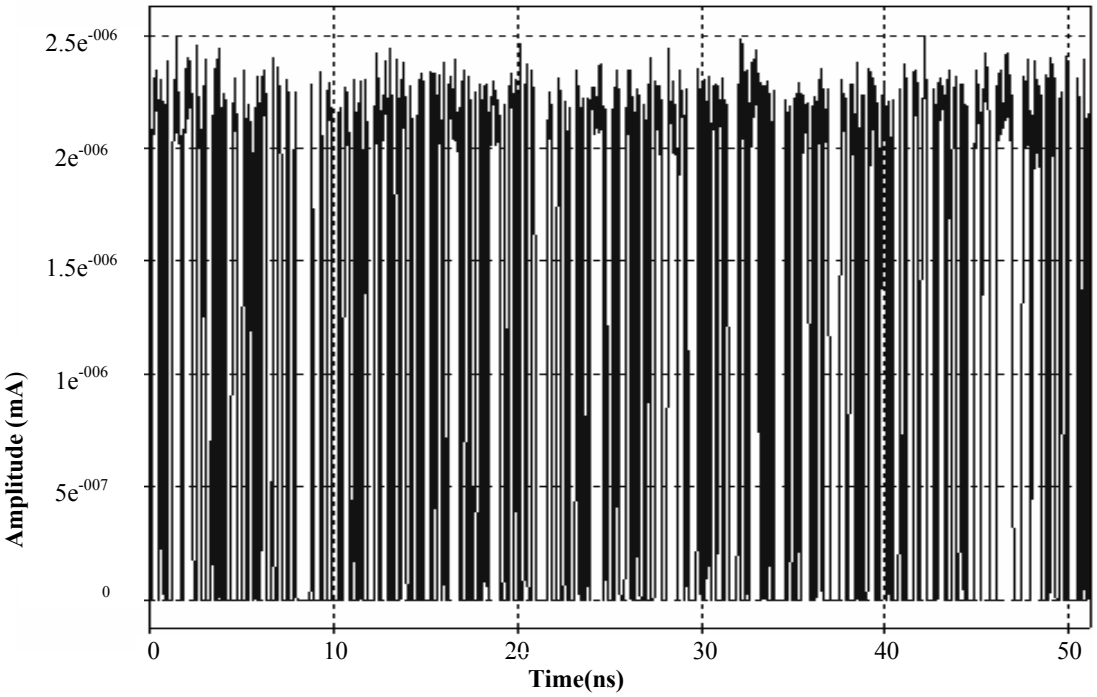

(a)

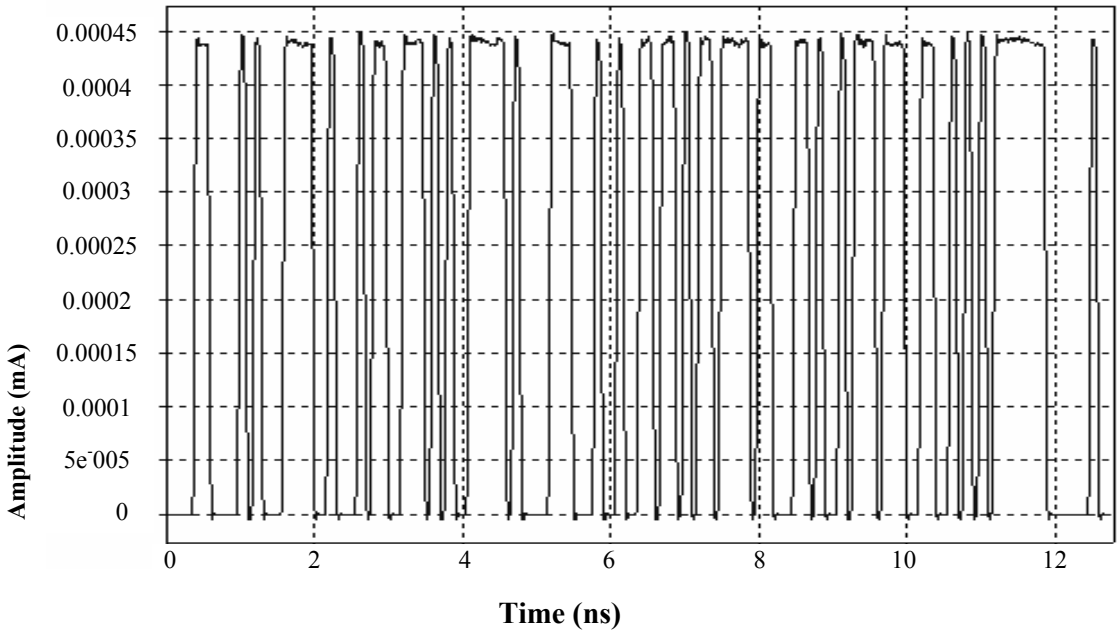

(b)

Figure 8. Electrical signal at the receiver (a) Fiber Bragg Grating & (b) Phase Conjugation

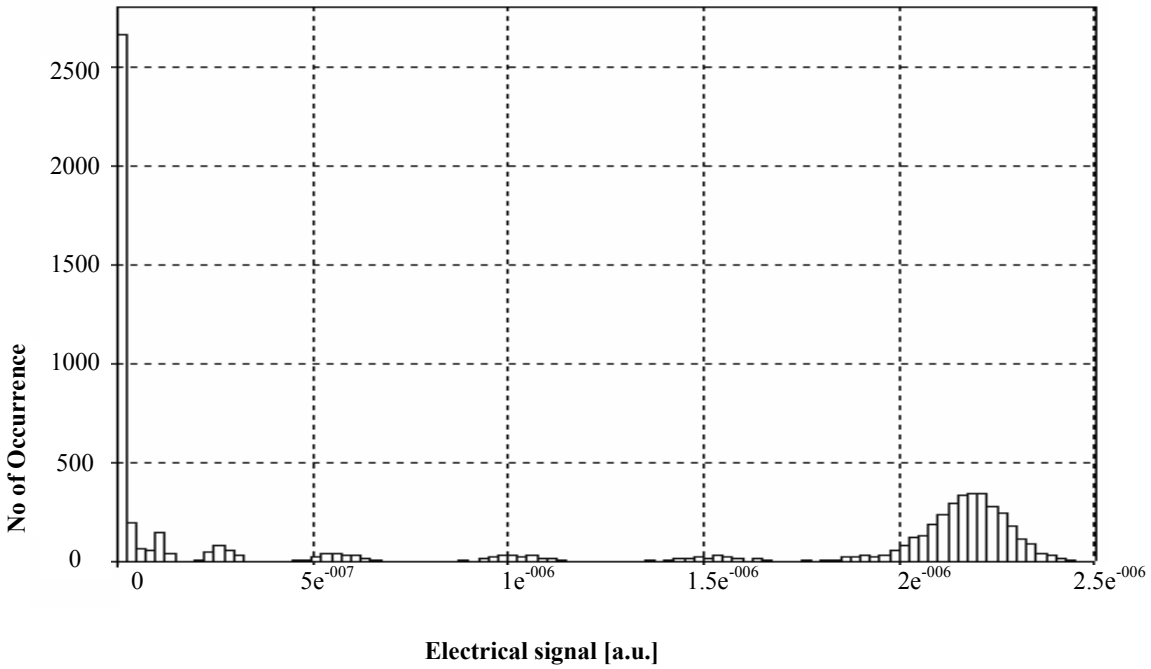

(a)

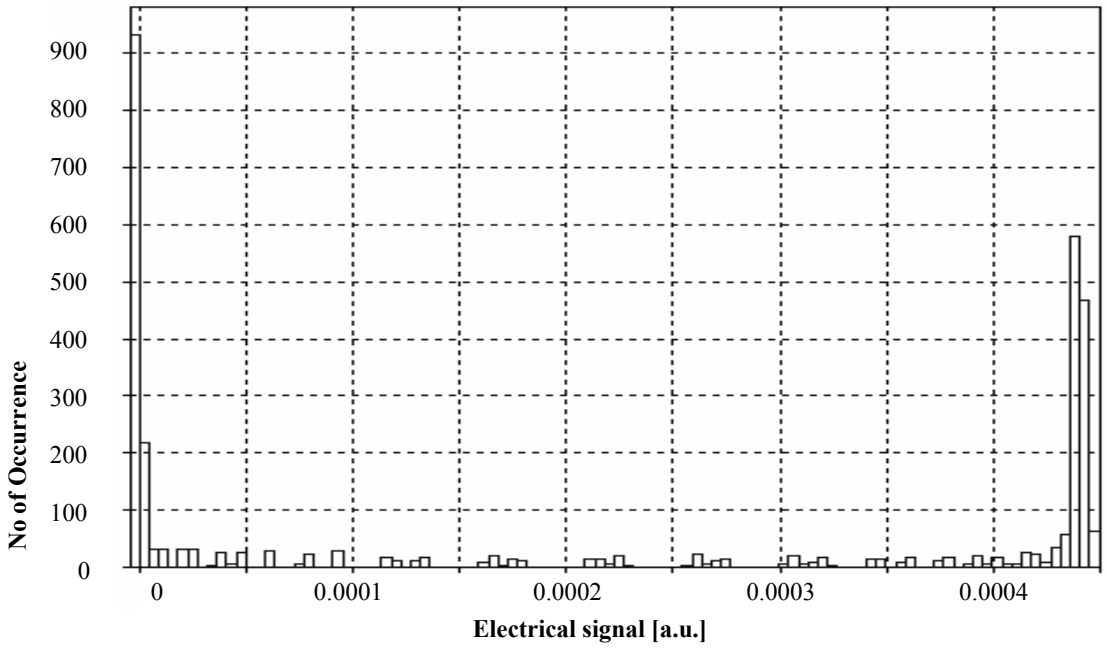

(b)

Figure 9. Corresponding histogram of electrical samples for the case (a) Fiber Bragg Grating & (b) Phase Conjugation

The schematic setup is given in Figure 3 and combines transmitter, a fiber span consisting of two links, a mid-span phase conjugator, and receiver. A 10 Gb/s NRZ data stream is sent over a first lossless fiber link here dispersion is set to D = 16 ps/nm-km. The peak power is set to -3 dBm. After 1000 km the eye diagram shows a completely closed eye, due to the accumulation of chromatic dispersion. Then the signal goes through an OPC,

and then to another 1000 km long fiber link [5]. At the output of the second link the received eye is completely open. Figure 8 & 9 demonstrates eye diagrams Electrical signal at the receiver & histogram of electrical samples

It is evident from Figure 9 (a) & (b) that the Corresponding histogram of electrical samples of OPC required less number of occurrence compared to FBG. From Figure 8 (a) & (b), it is clear that received electrical signal is very close to the original message signal by using OPC technique.

7. Conclusion

It is known from theory that a phase conjugator placed between two identical spools of fiber can completely compensate second-order dispersion. This theoretical result is confirmed by this numerical simulation. This dispersed signal is then being phase conjugated. The OPC reverses or inverts the optical spectrum of the signal so the shape of a pulse remains the same. Now the dispersion in the second half of the span reshapes the pulse so that, if the dispersion before the OPC matches the dispersion after it, then the original pulse shape will be restored at the end of the span. From the optical probes before and after the OPC shown in Figure 6 & 7, it can be seen that the phase conjugator near the center of the span reverses the broadening (spectral Inversion) and that this allows the broadening to be zero at the receiver and the pulse shape is restored to its input form. Since the signal spectrum after OPC becomes the mirror image of the input spectrum, by using an optical phase-conjugate (OPC) technique is also referred to as mid-span spectral inversion. It is obvious that the OPC technique has been found superior to the Fiber Bragg Grating (FBG) technique.

References

[1] Joseph C. Palais "Fiber Optic Communication System" Pearson Education Fourth Edition.2001.

[2] Nur Mohmmad, M.A.G. Khan, Toffawel Ahmed "Dispersion control of fiber optic cables by Fiber Bragg grating " Journal of Computer Science& Engineering CUET, Issue I, Volume I, 2008.

[3] J. M. Senior "Optical Fiber Communications", Principles and Practice, Prentice Hall, second edition, 1992.

[4] G. P. Agrawal "Nonlinear Fiber Optics", John Wiley & Sons, Inc. Third edition, 2003.

[5] J. Wilson, J.F.B. Hawkes, "Opto Electronics", Second edition, 2001.

[6] V. Rajaraman, "Fundamentals of Computers", Prentice-Hall of India, Fourth Edition, 2005-2006.

[7] http://www.rpphotonics.com/pulse_characterization.html

[8] http://en.wikipedia.org/wiki/Laser_diode

[9] http://www.opticsexpress.org/abstract.cfm

[10] Steven Lehar "An Intuitive Explanation of Phase Conjugation".http://cns-lumni.bu.edu/~slehar/webstuff/thesis/thesis.html

[11] http://Laserdiode-Wikipedia the free encyclopedia.htm

[12] S. M. A. Razzak ,Y . Namihira and M. A. G Khan "Optimum Ring Numbers in a Circular Photonic Crysstal Fiber (CPCFs)" 2005.

[13] Cucinotta, S. Selleri, L. Vincetti, and M. Zoboli, "Holey Fiber analysis through the finite element method," *IEEE Photon. Tech. Lett.* Vol. 14, pp.1530-1532, Nov. 2002.

Fully Coupled Time Domain Buffeting Analysis of Cable-Stayed Bridge

Md. Robiul Awall[1], Hiroki Yamaguchi[2], Tasnuva Humyra[1]
[1]Department of Civil Engineering, Rajshahi University of Engineering & Technology, Rajshahi – 6204, Bangladesh
robiul95@yahoo.com, robi95@gmail.com
[2]Department of Civil & Environmental Engineering, Saitama University, Japan

Abstract

Long-span cable-stayed bridges are prone to wind-induced vibration. Hence, the aerodynamic performance of such bridges in strong wind regions is of great concern. In this paper, analytical results of formulated fully coupled three-dimensional time domain buffeting analysis of a long-span cable-stayed bridge is presented. In the analytical work, the effect of spatial and temporal variation of wind speed and structural properties along the bridge deck has been taken into considerations. By using analytical approach wind-induced responses of the bridge deck, towers, and cables can be found simultaneously focusing inter-mode and multi-mode responses. Numerical study of a cable-stayed bridge has been carried out using the proposed approach and the results have been selectively presented.

1. Introduction

Cable-stayed bridge has become popular type of bridge throughout the world because of its aesthetic shape, structural efficiency, and economical construction. The increasing span lengths have been being used for the last 15 years ranging form 490*m* to 1088*m*. Recently China has built two world's longest cable-stayed bridges of lengths: 1018*m* and 1088*m* [1]. However, such a long span bridges are vulnerable to dynamic loads such as traffic, earthquakes and strong winds due to flexibility, low structural damping, deck shape and so on. After disaster of Tacoma narrow bridge in 1940, wind induced responses are considered in designing long span bridges such as suspension and cable-stayed bridges. Wind-induced vibrations of the bridge deck of a long-span cable-supported bridge are classified mainly as buffeting, vortex shedding, flutter and galloping. Many efforts have been made in last two decades to successfully prevent bridge deck from flutter instability and vortex-shedding response. Relatively less attention has been given to the buffeting response of bridge decks. The buffeting is defined as the wind-induced vibration in wind turbulence that generated by unsteady fluctuating forces as origin of the random ones due to wind fluctuations. The purpose of buffeting analysis is the prediction or estimation of total buffeting response of structures. Buffeting response prediction other than aeroelastic instability is of major concern in the wind resistance design and evaluation of wind-induced vibrations for long-span bridges. The buffeting response significantly increases with the increasing span lengths of modern long-span cable-supported bridges, which may lead to serious fatigue damage to structural components and connections, instability of vehicles traveling on the deck, and discomfort to pedestrian. Buffeting responses might also occur in construction stages where the partially erected structure is more flexible structure, i.e. the erection of the pylon [2].

In early 1960s, Davenport [3] applied statistical concepts of the stationary time series and random vibration theory to the buffeting analysis of long-span bridges. However, there remains some uncertainty over some of the functions used in the method. Davenport introduced aerodynamic admittance functions and joint acceptances to consider the temporal and spatial distributions of aerodynamic forces along the bridge deck. In the 1970s, Scanlan and Gade [4] extended their research results from flutter instability to buffeting response. Authors believed that aeroelastic forces in flutter instability would affect the buffeting response of the bridge deck, and hence authors suggested that the aerodynamic forces due to wind turbulence is to be considered together with the aeroelastic forces due to the motion of the deck in the buffeting analysis of the bridge. In the aerodynamic forces, however, authors did not consider the aerodynamic admittance functions.

The buffeting analysis of modern long-span bridges using either Davenport's theory or Scanlan's theory is actually a combination of numerical, experimental, and analytical approaches. Finite element technique is usually adopted to determine the natural frequencies and mode shapes of a modern long-span bridge. Modern long-span cable-supported bridges tend to have closely spaced natural frequencies. The contributions from multi-modes of vibration and inter-modes of vibration to the buffeting response, therefore, may have to be

considered. To consider the multi-mode buffeting response of a bridge deck, Lin and Yang [5] proposed a general linear theory for the computation of cross-spectra of the deck response to turbulent wind. Jain *et al*. [6] considered both multi-mode and inter-mode buffeting responses using a random vibration-based mode superposition approach. Katsuchi *et al*. [7] analyzed the Akashi-Kaikyo bridge, the longest suspension bridge in the world, using the multi-mode approach in reference [6] and demonstrated the significance of multi-mode responses of the bridge.

The wind-induced dynamic responses of bridge deck, towers and cables are traditionally determined separately to simplify the problem. Thus, wind-induced dynamic forces on the towers and cables are not considered in the aforementioned work. Recently, with respect to flutter instability of cable-stayed bridges, Ogawa *et al*. [8] pointed out that the ignorance of interaction between bridge deck, towers and cables may positively or negatively affect the prediction of flutter instability of a bridge. Davenport [9] also mentioned several possible mechanisms of interaction between the bridge deck and the cables. On the other hand, due to limitations in the frequency domain, it cannot reflect the entire response of bridge motions. Hence, it cannot supply enough information for the analysis of element fatigue and assessment of the degree of comfort of bridges under service loads. In the literature, several authors discussed time domain analysis of buffeting response [10-14]. However, those methods ignore the self-excited force and coupling between the modes of vibration.

In this paper, a new method is presented to analyze a fully coupled three-dimensional time domain buffeting of a long-span cable-stayed bridge. In this method, a three-dimensional finite element model of a cable-stayed bridge has been developed, which readily handle the bridge deck with significantly varying structural properties and mean wind speed along the deck. In addition, existing finite element models of the bridge for both static and eigenvalue analyses as well as the geometric nonlinearities can easily be incorporated in this new method. The present study includes inter-mode and multi-mode responses to determine wind-induced responses of the bridge deck, towers, and cables simultaneously.

2. Formulation of Motion Equation

The equation of motion for three-dimensional finite element model of long-span cable-stayed bridges for the buffeting response analysis can be expressed as

$$\mathbf{M}\ddot{\mathbf{Z}} + \mathbf{C}\dot{\mathbf{Z}} + \mathbf{K}\mathbf{Z} = \mathbf{F}_v\dot{\mathbf{Z}} + \mathbf{F}_d\mathbf{Z} + \mathbf{F}_b \tag{1}$$

Where, $\boldsymbol{Z}$ is the total nodal displacement vector including bridge deck, towers and cables (N dimensions), $\boldsymbol{M}$ is the mass matrix ($N\times N$ dimensions), $\boldsymbol{C}$ is the damping matrix ($N\times N$ dimensions), $\boldsymbol{K}$ is the stiffness matrix ($N\times N$ dimensions), $\boldsymbol{F_b}$ is the total Buffeting load vector acting on bridge deck, towers and cables (N dimension), $\boldsymbol{F_v}$, $\boldsymbol{F_d}$ are the motion-dependent unsteady aerodynamic force matrices associated with velocity and displacement (both are N dimension).

3. Finite Element Modeling of Cable-stayed Bridge

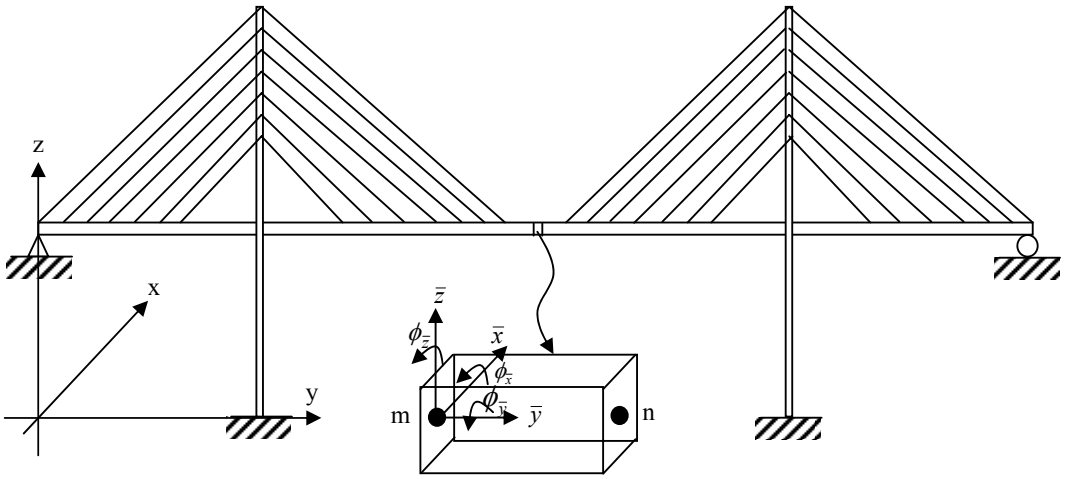

Figure 1. Cable-stayed bridge and its deck element

The bridge deck and towers of cable-stayed bridge are discritized as three dimensional beam elements having 12 degree of freedoms in local co-ordinate system. The displacement vector of the beam element can be written as

$$\mathbf{d}_{b\mathbf{i}}^{\mathbf{e}} = [\xi_m, \eta_m, \zeta_m, \phi_{\bar{x}m}, \phi_{\bar{y}m}, \phi_{\bar{z}m}, \xi_n, \eta_n, \zeta_n, \phi_{\bar{x}n}, \phi_{\bar{y}n}, \phi_{\bar{z}n}]^T \quad (2)$$

Cables are modeled by three-dimensional cable elements, composed of two nodes with total six degree of freedoms in local co-ordinate system as shown in Figure 2. Due to the very small bending stiffness, there is no bending moment. However, size of the element is small enough to minimize the sag effect of cable.

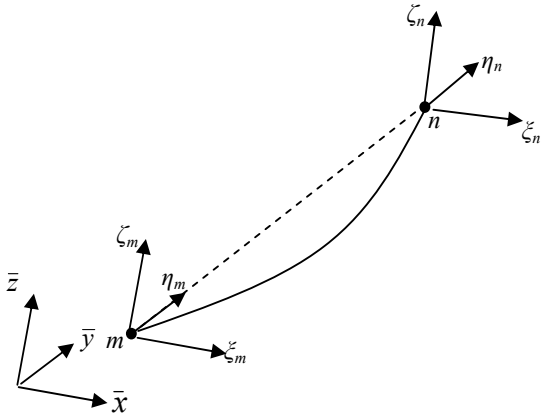

Figure 2. Cable element at local co-ordinate system

The displacement vector of the cable element can be written as

$$\mathbf{d}_{c\mathbf{i}}^{\mathbf{e}} = [\xi_m, \eta_m, \zeta_m, \xi_n, \eta_n, \zeta_n]^T \quad (3)$$

The relation between the internal displacements of the *i*th element and its nodal displacements can be expressed in general form as

$$\mathbf{d}_{\mathbf{i}} = \mathbf{B}_{\mathbf{i}}\mathbf{d}_{\mathbf{i}}^{\mathbf{e}} \quad (4)$$

Where, $\boldsymbol{d_i}$ is the internal displacement vector, $\boldsymbol{B_i}$ is the interpolation function matrix and $\mathbf{d}_{\mathbf{i}}^{\mathbf{e}}$ is the local nodal displacement vector of the *i*th element. For deck and tower element $\boldsymbol{d_{bi}^e}$ is the (12×1) local nodal displacement vector, $\boldsymbol{d_{bi}}$ is the (6×1) internal displacement vector, $\boldsymbol{B_{bi}}$ is the (6×12) interpolation function matrix of the *i*th beam element. Shape functions are cubic polynomials that must satisfy conditions on deflection as well as rotation at each end of the beam. Using Hermite's interpolation formula, interpolation function matrix can be expressed as follows.

$$\text{i.e. } \mathbf{d}_{b\mathbf{i}} = \begin{Bmatrix} \xi \\ \eta \\ \zeta \\ \phi_{\bar{x}} \\ \phi_{\bar{y}} \\ \phi_{\bar{z}} \end{Bmatrix}, \quad \mathbf{B}_{bi} = \begin{bmatrix} N_1 & 0 & 0 & 0 & 0 & N_2 & N_3 & 0 & 0 & 0 & 0 & N_4 \\ 0 & 0 & 0 & 0 & 0 & 0 & 0 & 0 & 0 & 0 & 0 & 0 \\ 0 & 0 & N_1 & -N_2 & 0 & 0 & 0 & 0 & N_3 & -N_4 & 0 & 0 \\ 0 & 0 & 0 & 0 & 0 & 0 & 0 & 0 & 0 & 0 & 0 & 0 \\ 0 & 0 & 0 & 0 & 1-\frac{y}{l} & 0 & 0 & 0 & 0 & 0 & \frac{y}{l} & 0 \\ 0 & 0 & 0 & 0 & 0 & 0 & 0 & 0 & 0 & 0 & 0 & 0 \end{bmatrix} \quad (5)$$

In which

$$N_1 = 1-3\left(\frac{y}{l}\right)^2 + 2\left(\frac{y}{l}\right)^3, \; N_2 = y\left(1-\frac{y}{l}\right)^2, \; N_3 = 3\left(\frac{y}{l}\right)^2 - 2\left(\frac{y}{l}\right)^3, \; N_4 = (y-l)\left(\frac{y}{l}\right)^2$$

For cable element $\boldsymbol{d_{ci}^e}$ is the (6×1) local nodal displacement vector, $\boldsymbol{d_{ci}}$ is the (3×1), internal displacement vector, $\boldsymbol{B_{ci}}$ is the (3×6) interpolation function matrix of the *i*th cable element

$$\text{i.e. } \mathbf{d}_{c\mathbf{i}} = \begin{Bmatrix} \xi \\ \eta \\ \zeta \end{Bmatrix}; \qquad B_{ci} = \begin{bmatrix} 1-\frac{y}{l} & 0 & 0 & \frac{y}{l} & 0 & 0 \\ 0 & 0 & 0 & 0 & 0 & 0 \\ 0 & 0 & 1-\frac{y}{l} & 0 & 0 & \frac{y}{l} \end{bmatrix} \quad (6)$$

4. Unsteady Aerodynamic Force

The unsteady aerodynamic forces per unit length of equation (1) are empirically obtained by wind-tunnel test with a section model.

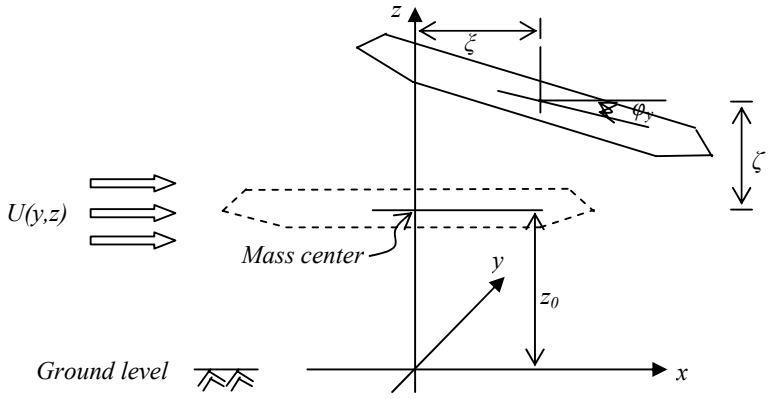

Figure 3. Section of a Bridge deck subjected to wind force

Bridge deck section subjected to the wind force in the global co-ordinate system is shown in Figure 3. Mean wind velocity (*U(y,z)*) is the function of *y* and *z*. Assume the deck is situated at constant distance (z_0) from the ground level and y axis lies along the deck length. So, the mean wind velocity that subjected to the bridge deck is as $U(y,z_0)$. Aerodynamic lift (F_L^{ae}) and moment (F_M^{ae}) associated with vertical (ζ) and torsional (φ_y) degrees of freedom are usually measured, but sometimes aerodynamic drag (F_D^{ae}) associated with lateral (ξ) degree of freedom also included in to measurement. Using the two dimensional derivation by Scanlan [16], three dimensionally motion-induced forces by considering strip assumption on the structure with constant mode shapes can be written as

$$F_D^{ae}=\frac{1}{2}\rho U^2(y,z_0)B_d\left[kP_1^*(k)\frac{\dot{\xi}}{U(y,z_0)}+kP_2^*(k)\frac{B_d\dot{\phi}_y}{U(y,z_0)}+k^2P_3^*(k)\phi_y+k^2P_4^*(k)\frac{\xi}{B_d}+kP_5^*(k)\frac{\dot{\zeta}}{U(y,z_0)}+k^2P_6^*(k)\frac{\zeta}{B_d}\right]$$

$$F_L^{ae}=\frac{1}{2}\rho U^2(y,z_0)B_d\left[kH_1^*(k)\frac{\dot{\zeta}}{U(y,z_0)}+kH_2^*(k)\frac{B_d\dot{\phi}_y}{U(y,z_0)}+k^2H_3^*(k)\phi_y+k^2H_4^*(k)\frac{\zeta}{B_d}+kH_5^*(k)\frac{\dot{\xi}}{U(y,z_0)}+k^2H_6^*(k)\frac{\xi}{B_d}\right]$$

$$F_M^{ae}=\frac{1}{2}\rho U^2(y,z_0)B_d^2\left[kA_1^*(k)\frac{\dot{\zeta}}{U(y,z_0)}+kA_2^*(k)\frac{B_d\dot{\phi}_y}{U(y,z_0)}+k^2A_3^*(k)\phi_y+k^2A_4^*(k)\frac{\zeta}{B_d}+kA_5^*(k)\frac{\dot{\xi}}{U(y,z_0)}+k^2A_6^*(k)\frac{\xi}{B_d}\right]$$

(7,a,b,c)

Where, F_D^{ae}, F_L^{ae} and F_M^{ae} are the aeroelastic drag, lift and torsional moment per unit length respectively, ρ is air density, B_d is deck width, $U(y,z_0)$ is mean wind velocity at z_0 height from the ground level, k $(=\omega B_d/U(y,z_0))$ is reduce frequency, ω is circular frequency, H_j^*, P_j^*, $A_j^*(j=1\text{-}6)$ are the flutter derivative. Since the aerodynamic derivatives depend on reduce frequency, the vibration frequency ω and flutter speed $U(y,z_0)$ should be estimated iteratively. Simplifying equation (7) by introducing the value of k and multiplying 2π and write in a matrix notation of element nodal forces in a local co-ordinate system is as below

$$\mathbf{F}_i^{ae}=\mathbf{F}_{\mathbf{v},i}^{ae}\dot{\mathbf{d}}_i+\mathbf{F}_{\mathbf{d},i}^{ae}\mathbf{d}_i \qquad (8)$$

Where, $\mathbf{F}_i^{ae} = \begin{Bmatrix} F_D^{ae} \\ F_{\bar{y}}^{ae} \\ F_L^{ae} \\ F_{M_{\bar{x}}}^{ae} \\ F_{M_{\bar{y}}}^{ae} \\ F_{M_{\bar{z}}}^{ae} \end{Bmatrix}$, $\dot{\mathbf{d}}_\mathbf{i} = \begin{Bmatrix} \dot{\xi} \\ \dot{\eta} \\ \dot{\zeta} \\ \dot{\phi}_{\bar{x}} \\ \dot{\phi}_{\bar{y}} \\ \dot{\phi}_{\bar{z}} \end{Bmatrix}$, $\mathbf{d}_\mathbf{i} = \begin{Bmatrix} \xi \\ \eta \\ \zeta \\ \phi_{\bar{x}} \\ \phi_{\bar{y}} \\ \phi_{\bar{z}} \end{Bmatrix}$

Here, $F_{\bar{y}}^{ae}$, $F_{M_{\bar{x}}}^{ae}$, $F_{M_{\bar{z}}}^{ae}$ are the force on $\bar{y}$ direction, moment on $\bar{x}$ and $\bar{z}$ directions in the local co-ordinate system.

$$\mathbf{F}_{\mathrm{v},i}^{ae} = \begin{bmatrix} C_1 P_1^* \frac{1}{B_d\omega} & 0 & C_1 P_5^* \frac{1}{B_d\omega} & 0 & C_1 P_2^* \frac{1}{\omega} & 0 \\ 0 & 0 & 0 & 0 & 0 & 0 \\ C_1 H_5^* \frac{1}{B_d\omega} & 0 & C_1 H_1^* \frac{1}{B_d\omega} & 0 & C_1 H_2^* \frac{1}{\omega} & 0 \\ 0 & 0 & 0 & 0 & 0 & 0 \\ C_2 A_5^* \frac{1}{B_d\omega} & 0 & C_2 A_1^* \frac{1}{B_d\omega} & 0 & C_2 A_2^* \frac{1}{\omega} & 0 \\ 0 & 0 & 0 & 0 & 0 & 0 \end{bmatrix}; \quad \mathbf{F}_{d,i}^{ae} = \begin{bmatrix} C_1 P_4^* \frac{1}{B_d} & 0 & C_1 P_6^* \frac{1}{B_d} & 0 & C_1 P_3^* & 0 \\ 0 & 0 & 0 & 0 & 0 & 0 \\ C_1 H_6^* \frac{1}{B_d} & 0 & C_1 H_4^* \frac{1}{B_d} & 0 & C_1 H_3^* & 0 \\ 0 & 0 & 0 & 0 & 0 & 0 \\ C_2 A_6^* \frac{1}{B_d} & 0 & C_2 A_4^* \frac{1}{B_d} & 0 & C_2 A_3^* & 0 \\ 0 & 0 & 0 & 0 & 0 & 0 \end{bmatrix}$$

In which $C_1 = \pi\rho B_d^3\omega^2$ and $C_2 = \pi\rho B_d^4\omega^2$

This unsteady aerodynamic force creates the aeroelastic stiffness and damping matrices which reduces the structural stiffness and damping. By using the principle of virtual work the aeroelastic stiffness and damping matrices of the *i*th element can be expressed as

$$\mathbf{C}_\mathbf{i}^{\mathbf{ae}} = \int_{l_i} \mathbf{B}_{b\mathbf{i}}^{\mathbf{T}} \mathbf{F}_{\mathbf{v},\mathbf{i}}^{\mathbf{ae}} \mathbf{B}_{b\mathbf{i}} d\bar{y} \quad \& \quad \mathbf{K}_\mathbf{i}^{\mathbf{ae}} = \int_{l_i} \mathbf{B}_{b\mathbf{i}}^{\mathbf{T}} \mathbf{F}_{d,\mathbf{i}}^{\mathbf{ae}} \mathbf{B}_{b\mathbf{i}} d\bar{y} \qquad (9,a,b)$$

Where, the integrals are definite integrals over the element length. If the length of the element is sufficiently small, the width of the element, the flutter derivatives, and the mean wind speed for the element can be regarded as constant with respect to the local co-ordinate $\bar{y}$. Thus after integration the above equation the aeroelastic element stiffness and aeroelastic damping matrices are 12×12 matrix and also element mass, damping and stiffness matrices size are 12×12 matrix. Since the unsteady aerodynamic force is a function of velocity and displacement, then re-arranging equation (1) gives

$$\mathbf{M}\ddot{\mathbf{Z}} + \mathbf{C}'\dot{\mathbf{Z}} + \mathbf{K}'\mathbf{Z} = \mathbf{F}_b \qquad (10)$$

Where, $\boldsymbol{C' = C - F_v}$, $\boldsymbol{K' = K - F_d}$

5 Buffeting Forces

A significant simplification in the case of bluff body flow is the so called quasi-steady theory. Here assuming that the oscillation frequency is much lower than the characteristic frequency of the flow and the aerodynamic forces at each instant are taken equal to those occurring in an equivalent steady situation, with the same relative motion between structure and flow. According to Simiu and Scanlan [16] the buffeting forces on the deck segment per unit length can be expressed as

$$F_{D_b}^d(t) = \frac{1}{2}\rho U^2(y,z_0) A_d [C_{Dd} \frac{2u(y,t)}{U(y,z_0)} + C_{Dd}^{'} \frac{w(y,t)}{U(y,z_0)}]$$

$$F_{L_b}^d(t) = \frac{1}{2}\rho U^2(y,z_0) B_d [C_{Ld} \frac{2u(y,t)}{U(y,z_0)} + (C_{Ld}^{'} + C_{Dd}) \frac{w(y,t)}{U(y,z_0)}]$$

$$F_{M_{yb}}^d(t) = \frac{1}{2}\rho U^2(y,z_0) {B_d}^2 [(C_{Md} + C_{Dd} \frac{A_d r}{B_d^2}) \frac{2u(y,t)}{U(y,z_0)} + C_{Md}^{'} \frac{w(y,t)}{U(y,z_0)}] \qquad (11,a,b,c)$$

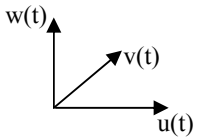

Where, C_{Ld}, C_{Dd}, C_{Md} are the steady wind force coefficient for lift force, drag force and moment of bridge deck respectively. $C' = \frac{dC}{d\alpha}$, A_d is projected area; r is distance of the loading point to the effective rotation axis. Assuming the buffeting forces act on steady state structures. But in real case structure is not steady state condition. That's why; introducing the aerodynamic admittance function in to above equation and buffeting forces are converted in to nodal buffeting forces as shown in the following matrix notation.

$$\mathbf{F_b^d} = \mathbf{G_b^d a^d} \tag{12}$$

In which

$$\mathbf{F_b^d} = \begin{Bmatrix} F_{D_b}^d(t) \\ F_{\bar{y}_b}^d(t) \\ F_{L_b}^d(t) \\ F_{M_{\bar{x}b}}^d(t) \\ F_{M_{\bar{y}b}}^d(t) \\ F_{M_{\bar{z}b}}^d(t) \end{Bmatrix}, \quad \mathbf{G_b^d} = \begin{bmatrix} 2R^d A_d C_{Dd} \chi_{Du}^d(f) & R^d A_d C_{Dd}' \chi_{Dw}^d(f) \\ 0 & 0 \\ 2R^d B_d C_{Ld} \chi_{Lu}^d(f) & R^d B_d (C_{Ld}' + C_{Dd}) \chi_{Lw}^d(f) \\ 0 & 0 \\ 2R^d B_d^2 [(C_{Md} + C_{Dd} \frac{Ar}{B_d^2}) \chi_{Mu}^d(f) & R^d B_d^2 C_{Md}' \chi_{Mw}^d(f) \\ 0 & 0 \end{bmatrix}, \quad \mathbf{a^d} = \begin{Bmatrix} \frac{u}{U} \\ \frac{w}{U} \end{Bmatrix}$$

Where, $\chi_{Lv}^d(f)$, $\chi_{Dv}^d(f), \chi_{Lv}^d(f)$, $\chi_{Lw}^d(f)$, $\chi_{Dw}^d(f), \chi_{Mw}^d(f)$ is the aerodynamic admittance of bridge deck, where the subscript two components associated with output and input components respectively and $R^d = \frac{1}{2}\rho U^2(y, z_0)$.

The consistent buffeting forces at the nodal points of the *i*th deck element can be obtain as

$$\mathbf{P_{i,b}^d} = \int_{l_i} \mathbf{B}_{bi}^{\mathrm{T}} \mathbf{G_{i,b}^d a_i^d} d\bar{y} \tag{13}$$

Buffeting forces on a bridge tower caused by along-wind and cross-wind turbulence and the aerodynamic coupling between lift and drag is ignored. According to Davenport [3] the buffeting forces on the bridge tower after introducing the aerodynamic admittance function and arranged as a matrix notation per unit length can be expressed as

$$\mathbf{F_b^t} = \mathbf{G_b^t a^t} \tag{14}$$

In which

$$\mathbf{F_b^t} = \begin{Bmatrix} F_{D_b}^t(t) \\ F_{\bar{y}_b}^t(t) \\ F_{L_b}^t(t) \\ F_{M_{\bar{x}b}}^t(t) \\ F_{M_{\bar{y}b}}^t(t) \\ F_{M_{\bar{z}b}}^t(t) \end{Bmatrix}, \quad \mathbf{G_b^t} = \begin{bmatrix} 2R^t B_t C_{Dt} \chi_{Du}^t(f) & R^t B_t C_{Dt}' \chi_{Dv}^t(f) \\ 0 & 0 \\ 2R^t B_t C_{Lt} \chi_{Lu}^t(f) & R^t B_t C_{Lt}' \chi_{Lv}^t(f) \\ 0 & 0 \\ 2R^t B_t^2 C_{Mt} \chi_{Mu}^t(f) & R^t B_t^2 C_{Mt}' \chi_{Mv}^t(f) \\ 0 & 0 \end{bmatrix}, \quad \mathbf{a^t} = \begin{Bmatrix} \frac{u}{U} \\ \frac{v}{U} \end{Bmatrix}$$

Where, $\chi_{Lv}^t(f)$, $\chi_{Dv}^t(f), \chi_{Mv}^t(f), \chi_{Lu}^t(f), \chi_{Du}^t(f)$, $\chi_{Mu}^t(f)$ is the aerodynamic admittance of bridge tower, where the subscript two components associated with output and input components respectively and $R^t = \frac{1}{2}\rho U^2(y_t, z)$

The consistent buffeting forces at the nodal points of the *i*th bridge tower element can be obtain as

$$\mathbf{P_{i,b}^t} = \int_{l_i} \mathbf{B}_{bi}^{\mathrm{T}} \mathbf{G_{i,b}^t a_i^t} d\bar{z} \tag{15}$$

According to quasi-steady assumption, the aerodynamic forces on cable segment per unit length due to turbulence are derived. The lift coefficients for circular cable section are to be zero and the mean wind velocity U_c is assumed constant through out the cable length. After introducing the aerodynamic admittance function and arranged as a matrix notation can be expressed as

$$\mathbf{F}_{\mathbf{b}}^{c} = \mathbf{G}_{\mathbf{b}}^{c}\mathbf{a}^{c} \tag{16}$$

In which

$$\mathbf{F}_{\mathbf{b}}^{c} = \begin{Bmatrix} F_{D_b}^{c}(t) \\ F_{\bar{y}_b}^{c}(t) \\ F_{L_b}^{c}(t) \end{Bmatrix}, \qquad \mathbf{G}_{\mathbf{b}}^{c} = \begin{bmatrix} 2R^{c}B_{c}C_{Dc}\chi_{Du}^{c}(f) \\ 0 \\ 2R^{c}B_{c}C_{Lc}\chi_{Du}^{c}(f) \end{bmatrix}, \qquad \mathbf{a}^{c} = \begin{Bmatrix} u \\ U \end{Bmatrix}$$

Where, $\chi_{Lv}^{c}(f)$, $\chi_{Dv}^{c}(f)$ is the aerodynamic admittance of cable, where the subscript two components associated with output and input components respectively and $R^{c} = \frac{1}{2}\rho U_{c}^{2}$.

Assuming the cable is modeled as a series of two node cable elements. The consistent buffeting forces at the nodal points of the *i*th bridge cable element can be obtain as

$$\mathbf{P}_{\mathbf{i,b}}^{c} = \int_{l_i} \mathbf{B}_{ci}^{\mathbf{T}}\mathbf{G}_{\mathbf{i,b}}^{c}\mathbf{a}_{\mathbf{i}}^{c}d\bar{y} \tag{17}$$

In which $\boldsymbol{B}_{ci}$ is the 3×6 interpolation function matrix for the cable element. The nodal buffeting forces obtained by equation (13), (15) and (17) are in the local co-ordinate systems. They are converted to the global co-ordinate system through the co-ordinate transformation matrix $\boldsymbol{T}_i$.

$$\mathbf{P}_{\mathbf{i,b}}^{\mathbf{s}} = \mathbf{T}_{\mathbf{i}}\mathbf{P}_{\mathbf{i,b}}^{e} \tag{18}$$

Where $\mathbf{P}_{\mathbf{i,b}}^{\mathbf{e}}$ can be forces on the deck element or tower element or cable element. $\mathbf{P}_{\mathbf{i,b}}^{\mathbf{s}}$ is the nodal force vector of the *i*th element in the global co-ordinate system. So the global force vector, including the bridge deck and towers and cables can be as

$$\mathbf{P}_{\mathbf{b}}^{\mathbf{s}} = \sum_{\mathbf{i}}^{\mathbf{n}} \mathbf{P}_{\mathbf{i,b}}^{\mathbf{s}} = \sum_{\mathbf{i}}^{\mathbf{n}} \mathbf{T}_{\mathbf{i}}\mathbf{P}_{\mathbf{i,b}}^{e} \tag{19}$$

6. Analytical Results

In buffeting response analysis, a cable-stayed bridge used by Das et *al*. [15] has been considered. The total length of the bridge is 689m with a main span of 371*m* as shown in Figure 4 and the properties of cable-stayed bridge are given in Tables 1 and 2.

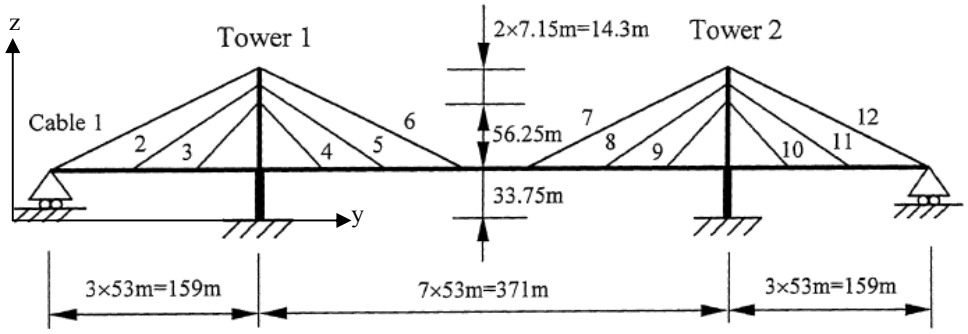

Figure 4. Cable-stayed bridge geometry

Table 1. Properties of deck and towers

Component	$A_{x\text{-}x}$ (m^2)	I_x (m^4)	E (MPa)	ρ_m (kg/m^3)
Deck	1.20	2.58	200000	11244
Tower above deck	14.2	30.0	31600	2449
Tower below deck	35.8	40.0	31600	2449

Table 2. Properties of stay cables

Cable No.	$A_{x-x}^{c}(m)^2$	E_c(MPa)	ρ_m^{c} (kg/m^3)
1, 12	0.060	165000	9438
2, 5, 8, 11	0.040	165000	9438
3, 4, 9, 10	0.028	165000	9438
6, 7	0.050	165000	9438

Cable-stayed bridge is modeled by ANSYS software, where deck and towers are modeled by beam element and cables are modeled by truss element shown in Figure.5. Considering many truss elements to model one cable to minimize the sag effect of cable. Nonlinear geometric effects are considered here. Eigenvalue analysis results are shown in Figure.6. All the natural frequencies below 2 Hz and their associated mode shapes were examined. First vibration mode is found in 0.39 Hz and second vibration mode of deck is found in 0.60 Hz. In these two frequencies deck, towers and cables are excited. Between these two frequencies there are four mode shapes are found where cables are excited itself. Hence the excitation of cable and tower are contributing the deck vibration.

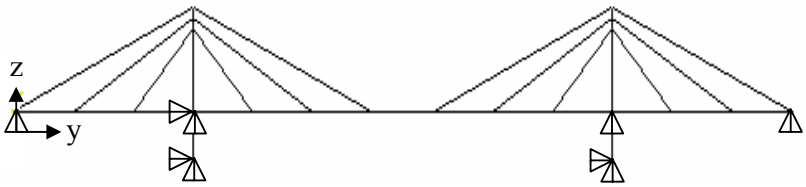

Figure 5. Model of Cable-stayed bridge

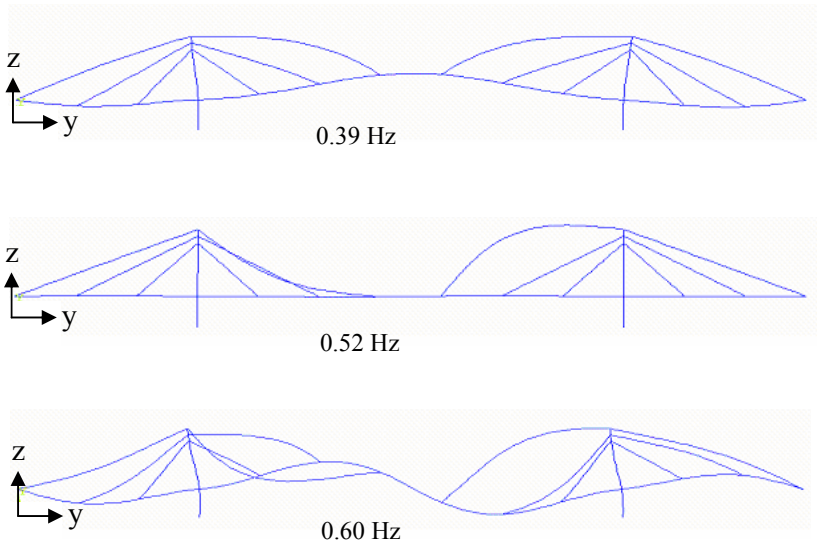

Figure 6. Eigenvalue analysis results of Cable-stayed bridge

Turbulence is generated from Kaimal [16] spectrum. Wind loads are converted into the time domain by using a computer simulation technique. Longitudinal and Vertical fluctuating components are given in Figure 7.

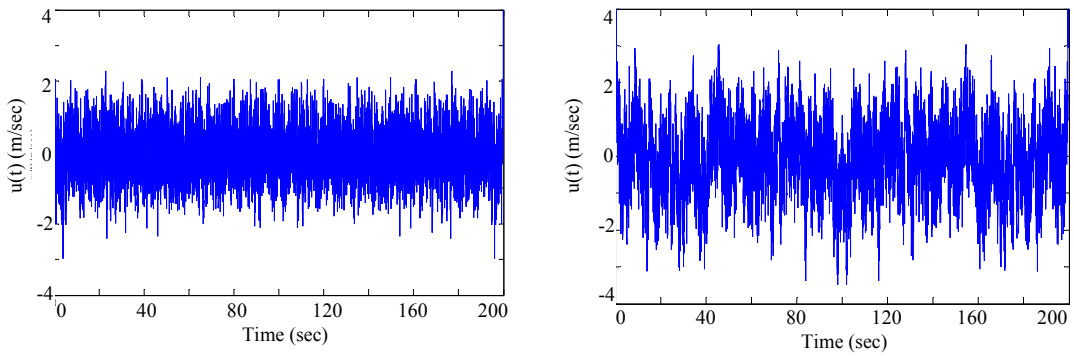

Figure 7. Simulated fluctuating wind component (a) Longitudinal (b) Vertical

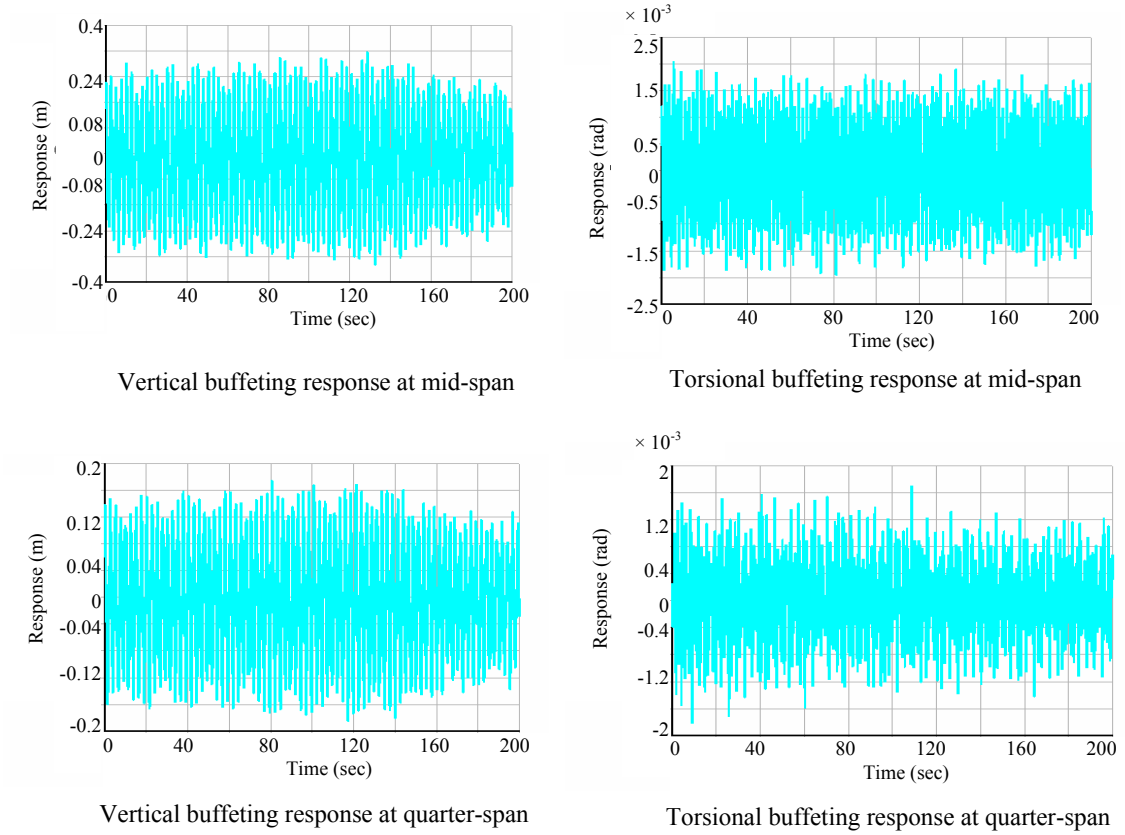

Figure 8. Time history of buffeting responses at mid and quarter span

A commercial FEM analysis software, ANSYS, was used to analyze the cable stayed bridge. The dynamic equation is solved by Newmark-β algorithm to calculate the buffeting response of the bridge including Rayleigh damping. Steady wind force co-efficient are usually determined by wind tunnel testing. In this case, values are assumed for some bridges wind tunnel test data [16-17]. The qualitative buffeting responses at the mid-span and quarter-span of cable-stayed bridge are computed under the mean wind speed of 50 m/s shown in Figure 8. From Figure 8, the behavior of buffeting response that occurs in the cable-stayed bridge can easily be understood. In case of vertical response, it can be seen that how responses are changing abruptly due to the random fluctuating force components. Torsional responses are more fluctuating than vertical responses. It is apparent that the response magnitude is dependent on the fluctuating component. Mid span response value is larger than the quarter span. These results are in good agreement with references [12-13].

7. Conclusions

An analytical approach has been presented in this paper for fully coupled three-dimensional time domain buffeting analysis of long-span cable-stayed bridges. The formulation is based on the finite element approach. The important features of the used approach are to readily handle the bridge deck of significantly varying structural properties and to make good use of the ready-made finite element models of the bridge for both static and eigenvalue analyses. In this formulation mean wind speed are vary with respect to space (horizontal and vertical direction) of deck and towers. By using suggested formulation wind-induced responses of the bridge deck, towers, and cables are find out simultaneously which naturally include inter-mode and multi-mode responses. Numerical study of a cable-stayed bridge has been carried out using the developed program and the results have been selectively presented. The case study, however, does not include effects of aerodynamic admittance, spatial correlation of flutter derivatives, aerodynamic forces and others which need further investigation.

8. References

[1] Y.J. Ge, H.F. Xiang, "Longest Chinese steel Bridges under construction", Proceeding of the China-Japan Joint Seminar on Steel and Composite Bridges, 12-22, 2007.

[2] L.M. Sun, Y.K. Wen, H.W. Hung, "Dynamic Behaviors and Vibration Control of Steel Tower of Long Span Cable-stayed Bridges under Construction", Proceeding of the Chaina-Japan Joint Seminar on Steel and Composite Bridges, 74-84, 2007.

[3] A. G. Davenport, "Buffeting of a suspension bridge by storm winds" Journal of Structural Division ASCE 88, 233-268, 1962.

[4] R. H. Scanlan and R. H. Gade, "Motion of suspended bridge spans under gusty wind" Journal of Structural Division ASCE 103, 1867-1883, 1977.

[5] Y. K. Lin and J. N. Yang, "Multimode bridge response to wind excitations" Journal of Engineering Mechanics ASCE 109, 586-603, 1983.

[6] A. Jain, N. P. Jones and R. H. Scanlan, "Coupled flutter and buffeting analysis of long-span bridges" Journal of Structural Engineering ASCE 122, 716-725, 1996.

[7] H. Katsuchi, N. P. Jones and R. H. Scanlan, "Multimode coupled flutter and buffeting analysis of the Akashi-Kaikyo bridge", Journal of Structural Engineering 125, 60-70, 1999.

[8] K. Ogawa, H. Shimodoi and H. Ishizaki, "Aeroelastic stability of a cable-stayed bridge with girder, tower and cables" Journal of Wind Engineering and Industrial Aerodynamics 41-44, 1227-1238, 1992.

[9] A. G. Davenport, "A simple representation of the dynamics of a massive stay cable in wind" AFPC Conference, Deauville, France, 427-437, 1994.

[10] Cheng Su, Xueming Fan, Tao He, "Wind-induced vibration analysis of a cable-stayed bridge during erection by a modified time-domain method", Journal of Sound and Vibration, 303, 330-342, 2007

[11] X. Chen, A. Kareem, "Discussion on Time domain buffeting response calculations of slender structures", Journal of Wind Engineering and Industrial Aerodynamics,90, 639-642, 2002.

[12] C. Liu, H. Xiang, "Simulation of buffeting response history for long span bridges", 8th ASCE Special Conference on Probabilistic Mechanics and Structural Reliability, PMC2000-159, 1-6, 2000.

[13] W. W. Yang, C.C. Chang and T.Y.P. Chang, "Time domain buffeting analysis of cable-supported bridges", 2nd Int'l Symp. on Civil Infrastructure Systems, 27-34, December, 1996.

[14] Q. Ding, P.K.K. Lee and S.H. Lo, "Time domain buffeting analysis of suspension bridges subjected to turbulent wind with effective attack angle", Journal of Sound and Vibration, 233(2),311-327, 2000.

[15] A. Das, A. Dutta, S. Talukdar, "Efficient dynamic analysis of cable-stayed bridges under vehicular movement using space and time adaptivity", FE in Analysis and Design, 40, 407-424, 2004.

[16] Emil Simiu, Robert H. Scanlan, Wind Effects on Structures: An Introduction to Wind Engineering, Wiley-Inter-Science, 2nd Edition, 1-604, 1986.

[17] Claes Dyrbye, Svend O. Hansen, Wind loads on structures, John wiley & sons, 1st edition, 1-229, 1999.

Liquid Fuel Production from Sugarcane Bagasse by Fluidized Bed Pyrolysis Technology

Mohammad Rofiqul Islam*, Md. Shazib Uddin and Mohammad Nurul Islam
Department of Mechanical Engineering, Rajshahi University of Engineering & Technology, Rajshahi-6204, Bangladesh
*E-mail: mrislam1985@yahoo.com

Abstract

The conversion of sugarcane bagasse into pyrolytic oil by fluidized-bed reactor has been taken into consideration in this study. The bagasse in particle form was pyrolyzed in an externally heated 7cm diameter and 37.5cm high fluidized-bed reactor with nitrogen as a carrier gas. The reactor chamber and gas-preheater were heated by means of a renewable energy biomass source cylindrical heater. At a reactor bed temperature of 450℃ for a feed particle size of 420-600μm and at a gas flow rate of 30 l/min, an oil yield of 48wt% of dry feed was obtained. The pyrolysis process temperature was found to have influenced on the product yields. The product oil was analyzed for their properties as an alternative fuel and compared with other biomass derived pyrolysis oil and petroleum product. The fuel properties compared were physical properties, calorific value, elemental (CHNOS) analysis and chemical composition using Fourier Transform InfraRed (FT-IR) spectroscopy. The properties found to be comparable with other biomass derived fluidized fuels.

Keywords: Fluidized-bed pyrolysis, Sugarcane bagasse, Liquid fuel, FT-IR

1. Introduction

Pyrolysis for energy conversion from carbonaceous wastes is defined as the thermal degradation of organic matter either in total absence of air or with a lack of a stochiometrically needed amount of oxygen to the extent where gasification does not occur. Pyrolysis processes are usually conducted in a reactor where heat is applied to the feedstock either externally or by the partial combustion of the feedstock. Three products are usually obtained in a pyrolysis process: liquid, solid char and gas. When the organic matter is heated in an inert atmosphere the primary vapors are first produced, the characteristics of which are most influenced by heating rate. These primary vapors then further degrade to secondary tars and gases if held at high temperature for long time for secondary reaction to occur. The proportions and characteristics of the secondary material are a function of temperature and time. Rapid quenching causes the liquid intermediate products of pyrolysis to condense, before further reaction breaks down the higher molecular weight species into gaseous products. The conventional sources of fossil fuels have been depleting at an alarming rate and hence the focus on alternative renewable source of energy is increasing. As a result biomass as a renewable energy source has continued to attract increased attention [1, 2]. A lot of work in this area is in progress using different biomass solid waste as the feed material [1-8]. Sugarcane grows in many parts of the tropical climate in the world. About 20wt% of raw sugarcane is generated as biomass solid waste in the form of sugarcane bagasse (sun-dry basis). There are 17 sugar mills in Bangladesh and the bagasse is the major by-product of these mills. Some amount of the by-product is used as fuel for boiler in the millhouse. Mostly this is either under-utilized or unutilized as a source of heat energy. For the past five years the generation of this waste was 1489.2, 1433.0, 1504.2, 1475.8 and 1390.2 thousand metric ton, respectively [9]. It is creating waste management problem, especially in the sugar milling sites. Thus, an endeavor from the point of view of the energy recovery from this sugarcane bagasse waste by thermo chemical process may be worthwhile. Characterization studies on solid sugarcane bagasse have been carried out through proximate, ultimate and thermo gravimetric (TG) analysis [10]. The results of these analyses showed that the solid biomass has high potentials to provide liquid fuel by pyrolysis conversion process. Amongst the thermo chemical processes, pyrolysis has received increasing attention since the process conditions may be optimized to produce high energy density pyrolytic oil in addition to the derived char and gas [2]. The pyrolytic oil may be used directly as a fuel, catalytically upgraded to refined fuel, or added to petroleum refinery feed stocks [2, 3]. The solid char may be useful as fuel, either directly, briquetted or as char-oil or char-water slurries [2]. In addition the derived gas has a high calorific value sufficient to be used for total energy requirements of the biomass pyrolysis plant [2, 4]. Consequently all the derived product streams from the pyrolysis of biomass are available for recovery of energy. Some works have been carried out with the sugarcane

bagasse as feedstock at the Fluid Mechanics Laboratory of the Department of Mechanical Engineering, Rajshahi University of Engineering & Technology to obtain liquid fuel using fluidized-bed pyrolysis technology.

2. Materials and Methods

2.1. Biomass

The bagasse was collected from Rajshahi Sugar Mills Limited, Horian, Rajshahi, Bangladesh. It was ground and sieved to the size ranges of 0-150, 150-300, 300-420, 420-600, 600-1180μm and finally dried for 24 hours at 110°C prior to pyrolysis. The gross calorific value of the solid sugarcane bagasse is 16.81 MJ/kg. The proximate and ultimate analysis of the solid biomass is presented in Table 1.

Table 1. Proximate and ultimate analysis of solid sugarcane bagasse

Proximate analysis		Ultimate analysis	
Contents	Wt%	Elements	wt%
Volatile	74.98	C	43.77
Fixed carbon	13.57	H	6.83
Moisture	9.51	N	-
Ash	1.94	O	47.46
		S	-

2.2. Experimental system

The experimental system was a fluidized bed pyrolysis unit. Nitrogen gas was used as fluidizing gas to make the system inert and dry silica sand was used as bed material. The sand in the fluidized bed was of mean size 181μm diameter with static bed height of 5cm. The flow diagram of the pyrolysis conversion system is presented in Figure 1. The schematic diagram of the experimental system is presented in references [11-12]. The reactor was 7 cm (diameter), 37.5 cm (height), constructed of stainless steel with full gas flow and temperature control. The reactor was heated externally. The incoming fluidizing nitrogen gas was pre-heated before entering into the reactor in a pre-heating chamber. The fluidizing gas flow rate was measured and controlled by nitrogen gas flow meter and flow control valve, respectively. The reactor bed and gas pre-heating chamber were heated by means of renewable energy biomass burning cylindrical heater. A blower supplied air required for burning biomass in the heater. By varying the air supply that was directly related to the blower speed, the temperature of the reactor was controlled. The temperature in the fluidized bed reactor was measured by a digital pyrometer. The gravity feed type heater feeder supplied the heater biomass required for continuous heating of the reactor. The ash of burned biomass in the heater was disposed through the ash disposal system at the bottom of the heater due to gravitational force only. Exhaust gas due to burning of heater biomass was exhausted into the atmosphere through a pipeline at the top of the heater. The biomass solid waste particles were fed into the reactor by a gravity feed type reactor feeder. The feed rate was maintained near about constant by a feed control valve at the bottom of the reactor feeder. Gravitational force was the main agent for feeding the reactor. The system was maintained at a pressure slightly above atmospheric by a nitrogen gas pressure regulator. The char was collected from the reactor after completing a run. The vapors and gases were passed through a water-cooled condenser to a series of two ice-cooled collectors to trap the derived liquid product. The fluidizing gas and noncondensible vapor were flared into the atmosphere. In this experimental study, the influence of reactor bed temperature, fluidizing gas flow rate and feed particle size on the product yields were studied. The reactor bed temperature was varied from 400°C to 500°C at an interval of 25°C while the fluidizing gas flow rate was varied from 22 to38 l/min at an interval of 4 l/min.

2.3. Oil product analysis

2.3.1. Physical and chemical analysis

The pyrolytic oil obtained at the maximum liquid yield condition was characterized for its physical and chemical properties. These properties were determined according to standard American Society for Testing and Materials (ASTM) test methods. The properties determined were: kinematic viscosity, density, pH value, flash point, pour point and gross calorific value. The elemental composition by ultimate analysis, in terms of carbon, hydrogen, nitrogen, oxygen and sulfur (CHNOS) content of the oil was determined. The test was carried out by

an Elemental Analyzer of model EA 1108 according to the ASTM D3176-84 standard test procedures in the laboratory of Analytical Research Division, Bangladesh Council of Science and Industrial Research (BCSIR), Dhaka. The technique used for the determination of CHNS was based on the quantitative "Dynamic Flash Combustion" method. The oxygen content was determined by difference, knowing the ash content.

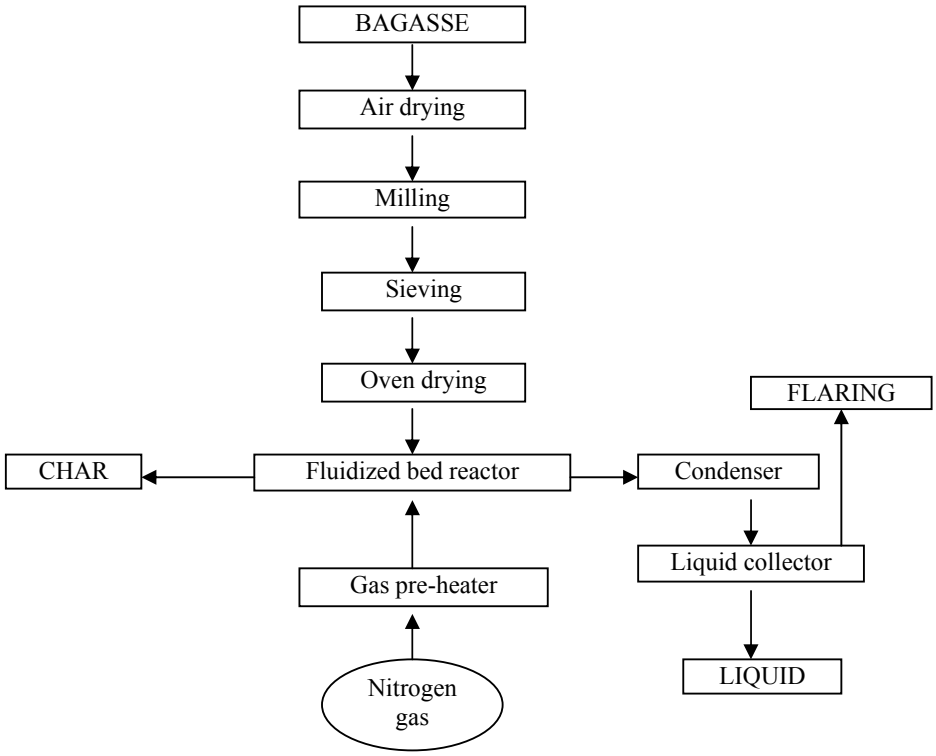

Figure 1. Flow sheet of fluidized-bed pyrolysis system

2.3.2. Compositional analysis

The functional groups of the pyrolysis liquid obtained at reactor bed temperature of 450°C were analyzed by Fourier Transform InfraRed (FT-IR) spectroscopy to identify the basic compositional groups. The FTIR instrument of model SHIMADZU FTIR 8400 was used to produce the ir-spectra of the derived oil. A thin uniform layer of the liquid was placed between two salt cells and exposed to infrared beam. In the FTIR 8400, the infrared beam from light source was reflected by Collimator Mirror into the interferometer. A parallel beam entered the Michelson interferometer with a 30° incident angle. The beam was then divided by beam Splitter, the resultant beams falling upon moving mirror and fixed mirror. Both beams were reflected back to the beam splitter and joined into one interference beam before proceeding to collecting mirror. From the collecting mirror, the parallel infrared beam created an image of the light source in the center of the sample compartment. Another collecting mirror gathered the beam that passed through the sample and reflected it to detector as the interferogram. After reaching the detector, the interferogram underwent several treatments before being sent to the computer. It was amplified by the preamplifier and the automatic gain amplifier, passed through high-pass and low-pass filters, and was digitized by the 20-bit A/D converter. After the signal was digitized into the interferometer memory, it traveled through the SCSI interface to the PC where Hyper-IR transformed the interferogram into a spectrum. It provided the absorption spectrum in percentage incident intensity, along the wave numbers 4000 to 500 cm^{-1}. The standard ir-spectra of hydrocarbons were used to identify the functional group of the components of the derived liquid. The test was conducted in the laboratory of Department of Chemistry of Rajshahi University, Bangladesh.

3 Results and Discussions

3.1. Product yields

Three common products: oil, char and gas were recovered after each run of sugarcane bagasse pyrolysis. Higher percentage of liquid collection makes this biomass potential for liquid fuel extraction. The liquid appeared brownish dark with a strong acrid smell. Careful handling of the liquid was required since the liquid reacted easily with human skins, leaving permanent yellowish brown marks and an acrid smell for a few days, which cannot be removed by detergent. No phase separation was found to take place. The liquid product was collected in two ice-cooled liquid collectors in series. The char was collected from the reactor. This char were expected to be very reactive, and precautions were required to ensure that it would not be exposed to air when still hot. The gas was diluted by the large flow of nitrogen gas and flared into the atmosphere.

3.2. Effect of reactor temperature

Figure 2 shows the variation of percentage mass of liquid, char and gaseous products at different reactor bed temperature for bagasse pyrolysis with particle size 420-600μm, fluidizing gas flow rate of 30l/min. From this figure, it is found that the maximum liquid product yield was obtained at a reactor bed temperature of 450°C and this was 48wt% of total biomass fed. With the decrease of bed temperature at 400°C, the liquid product yield was decreasing (39wt% of biomass fed) while with the increase of bed temperature at 500°C the liquid product yield was again decreasing (38wt% of biomass fed). With the increase of reactor bed temperature, the solid char yield was decreasing for the temperature range of 400°C to 500°C. For feed particles of size 420-600μm, a bed temperature of 400°C yielded the maximum percentage mass of char, 49wt% of biomass fed. At a higher temperature of 500^0C, the solid char production was lower, it was found to be 32wt% of biomass fed. Figure 2 also shows that as the reactor bed temperature was increased the gaseous product yield was increasing. A fluidized bed temperature of 500°C yielded the maximum percentage mass of gas yield of 30wt% of biomass fed. The gas yields were near to minimum at the condition of maximum oil production.

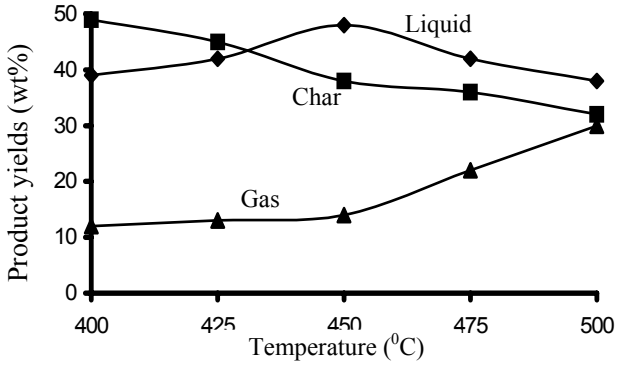

Figure 2. Effect of reactor bed temperature on product yields for feed size of 420-600 μm and gas flow rate of 30 l/min.

This is supported by the thermogravimetric (TG) study of solid sugarcane bagasse, where the complete devolatilization of volatile in bagasse was found to take place at around 450°C. The reason for lower liquid product yield at lower bed temperature may be due to the fact that the temperature rise was not sufficient enough for complete pyrolysis to take place yielding less liquid product and higher char production. On the other hand at higher reactor bed temperature there was a possibility of secondary decomposition reactions to take place in the reactor rendering lower liquid and higher amount of gas.

3.3. Effect of feed particle size

Figure 3 represents the percentage yield of liquid and solid char products for different particle size of bagasse at a fluidized bed temperature of 450ºC and fluidizing gas flow rate of 30 l/min. It was observed that at a

fluidization gas flow rate of 30 l/min, the percentage yield of liquid product was maximum, 48wt% of total biomass fed for particle size of 420-600µm with a solid char product of 37wt% of dry biomass fed. The particle of size less than 150µm produced a percentage yield of liquid product of 32wt% of dry biomass fed with a solid char product of 42wt% of biomass fed. The large particle of size 600-1180µm produced percentage yield of liquid and char products of 46 and 41wt% of biomass fed, respectively.

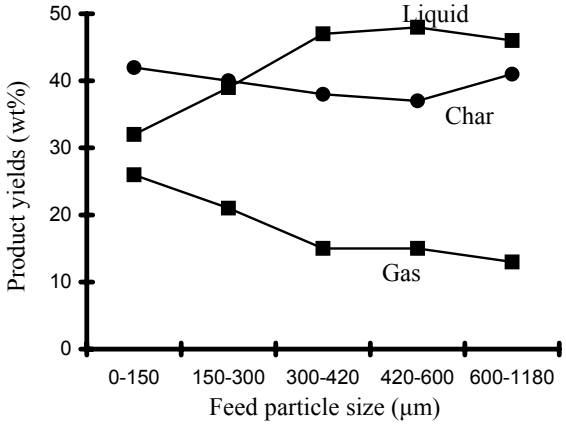

Figure 3. Effect of feed particle size on product yields for bed temperature 450^{0}C and gas flow rate of 30 l/min.

This may be due to the fact that the smaller size particles were either overheated, or too quickly blown from the reactor before commencing pyrolysis completely with producing more char. On the other hand, the larger size particles were not adequately heated up so rapidly causing incomplete pyrolysis rendering reduced liquid product yield. With the increase of feed particle size, gas yield was decreasing from 26 to 13wt% of biomass fed.

3.4. Effect of fluidizing gas flow rate

Figure 4 shows the variation of percentage yield of liquid, solid char and gas product at a reactor bed temperature of 450°C for feed particle of size 420-600µm. The maximum liquid product was 48 wt% of biomass fed while the solid char product was 36wt% of dry fed at a fluidization gas flow rate of 30 l/min. It was observed that at the beginning with lower fluidization gas flow rate at 22 l/min, the liquid product was 35wt% of biomass fed with a char product of 38wt% of biomass fed and a gas yield of 27wt%.With the increase of fluidization gas flow rate up to 30 l/min,the liquid product was increasing with a decreasing trend of gas yield. The char yield appeared to be more or less constant. This may be due to the fact that at lower fluidization gas flow rate the fluidization was not achieved completely and hence, the fast pyrolysis reaction could not take place properly. At higher gas flow rate, the fluidization was good enough for high heating rate causing fast pyrolysis for maximum liquid yield and the vapor residence time was quite low which was not enough for secondary reaction to take place yielding less gas and more liquid product. When the fluidization gas flow rate was increased to values higher than 30 l/min, char particles of 420-600µm size feed particles were found to be elutriated significantly into liquid collector, thus disturbing the system as a whole.

3.5. Product oil characteristics

3.5.1. Physical and chemical characteristics

The elemental composition and the physical characteristics of the bagasse pyrolysis oil obtained at the maximum yield temperature of 450°C is shown in Table 2. The energy content of the oil was 19.185 MJ/kg, due to the presence of moisture and oxygenated compounds. However, it was significantly higher than that of raw

bagasse. The oil was heavier than water with density at 30°C is 1160 kg/m^3 and hence, results higher volumetric energy content. The flash point of the oil was 103°C hence, precautions are not required in handling and storage at normal atmosphere. The oil was easily pourable and the pour point was low, less than –16°C. The oil was found to be moderate in viscosity. The liquid was very acidic with low pH value of 2.98 suggesting its corrosive in nature.

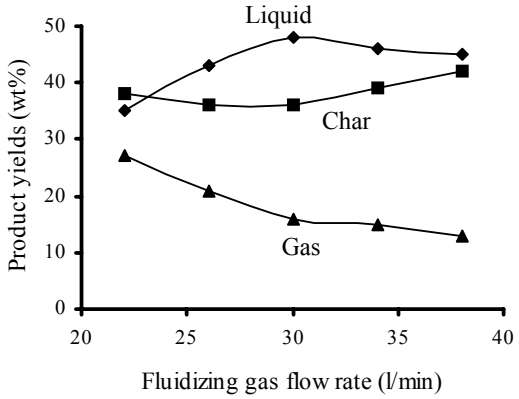

Figure 4. Effect of fluidizing gas flow rate on product yields for particle size of 420-600 µm and bed temperature of 450°C.

Table 2. The elemental composition and physical characteristics of the bagasse pyrolysis oil and its comparison

Analyses	Standard	Bagasse	Wood waste [5]	Fast diesel [13]
Elemental (wt%)				
C	ASTM D3176-84	45.01	46.24	86.10
H	ASTM D3176-84	6.00	7.55	12.80
N	ASTM D3176-84	-	0.141	-
S	ASTM D3176-84	-	0.03	0.5
Ash	ASTM D482-IP 4	0.25	0.04	0.01
O	By difference	48.74	46.00	-
Viscosity @ 30^{o}C (cSt)	ASTM D445-IP71	13.80	66.99	1.3-3.3
Density (kg/m^3)	-	1160	1180.2	780
pH value	Digital pH meter	2.98	2.8	-
Flash point (°C)	ASTM D92-IP 36	103	59	75
Pour point (°C)	ASTM D97-IP 15	-16	-	-
GCV (MJ/kg)	DIN 51900	19.185	19.80	45-46

The elemental analysis of the oil is an important criterion for the design of a combustion plant utilising the oil with the help of the elemental analysis, the combustion calculation can be carried out from which the quantities of combustion air and flue gas and also the composition of the flue gas can be determined [6]. Bio-crude oils have some properties that are quite different from those of petroleum-derived oils. Biocrude oils contains a large amount of oxygen. The oxygen content of bio-oils (excluding water) is a function of the oxygenated feedstock from which they are made, as well as the residence time and temperature of the pyrolysis step [7]. The oxygen content in the liquid was 48.74%, calculated by difference, was close to that of feedstock composition. The sulfur content of bio-oils is naturally low, due to the low sulfur content of biomass. This low sulfur content is one of the positive aspects of bio-oils [7]. The amount of sulfur in the biomass derived oils will indicate the quantity of the hazardous SO_2 emission in combustion processes. The sulfur was not found and ash content was also found to be low as 0.25% of the oil weight. One of the variables with bio-oils will be the nitrogen content of the oil, which will reflect the variable protein content possible with biomass. Biomass which has a significant content of green, living plant cells (e.g. green grasses) will have a higher nitrogen content than biomass having a

large content of dead plant cells (e.g. straw and wood) [7]. The nitrogen content in the bio-oils will contribute to NO_x emissions and it was not detectable in the sugarcane bagasse pyrolytic product.

3.5.2. Compositional analysis

From the Fourier transform infra-red spectroscopy of the derived pyrolytic oil, the FTIR functional groups and the indicated compositions of the liquid product were presented in Table 3. The presence of water impurities and other polymeric O-H in the oil are indicated by the broad absorbance peak of O-H stretching vibration between 3600 and 3200 cm^{-1}. The presence of alkenes were indicated by the strong absorbance peak of C-H vibrations between 3050 and 2800 cm^{-1} and the C-H of deformation vibrations between 1490 and 1325cm^{-1}. The absorbance peaks between 1775 and 1650 cm^{-1} represented the C=O stretching vibration, indicating the presence of ketones, aldehydes and carboxylic acids. The possible presence of alkenes were indicated by the absorbance peaks between 1680 and 1575 cm^{-1} representing C=C stretching vibrations. The sharp but less prominent absorbance peaks between 1550 and 1475 cm^{-1} represented $–NO_2$ stretching vibration indicated the presence of small nitrogenous compounds. The overlapping peaks between 1300 and 950 cm^{-1} were suggested due to the presence of primary, secondary and tertiary alcohols, ethers and esters due to the C-O stretching and O-H deformation vibration of these functional groups. Absorbance peaks between 900 and 650 cm^{-1} indicated the possible presence of single, polycyclic and substituted aromatics groups. These functional groups and the indicated composition have been identified in the pyrolytic derived oils from rice-husk from fluidized bed reactor by Islam and Ani [1]. The pronounced oxygenated functional groups of O-H; C=O; C-O and aromatic compounds showed that the oil was highly oxygenated and therefore very acidic, as have also been indicated by the elemental composition and the pH value. The high fraction of oxygenated compounds reduces the calorific value of the oil since C=O bonds do not release energy during combustion. The presence of hydrocarbon groups C-H; C=C; and alcohols indicate that the liquid has a potential to be used as fuel.

Table 3. FT-IR functional groups and the indicated compounds of the pyrolysis oil

Frequency range (cm^{-1})	Groups	Class of compounds
3600-3200	O-H stretching	Polymeric O-H, water impurities
3050-2800	C-H stretching	Alkanes
1775-1650	C=O stretching	Ketones, Aldehydes, Carboxylic acids
1680-1575	C=C stretching	Alkenes
1550-1475	-NO_2 stretching	Nitrogenous compounds
1490-1325	C-H bending	Alkanes
1300-950	C-O stretching	Primary, secondary and tertiary alcohols, phenol, esters, ether
900-650	O-H bending	Aromatic compounds

4. Conclusions

Fluidized-bed pyrolysis of solid sugarcane bagasse had given maximum oil yield that was 48wt% of biomass fed at a reactor bed temperature of 450°C and at a fluidizing gas flow rate of 30 l/min. With increasing reactor bed temperature, the percentage mass of char production was decreasing while gas production was increasing.

- The pyrolytic oil was a single-phase liquid product.
- The elemental composition of the oil was better than that of solid biomass.
- FT-IR analysis showed that the liquid was dominant with oxygenated species.
- The physical properties analysis showed that the oil was heavy and acidic in nature with moderate viscosity. The oil possessed favorable pour and flash points.
- The heating value of the oil was moderate, however, the value is similar to other biomass derived pyrolytic oil. This value was significantly higher than that of solid bagasse.

Acknowledgements

The authors wish to thank the Ministry of Science and Technology of Government of People's Republic of Bangladesh for providing the financial support for the research work. Thanks are due to the Institute of Fuel Research and Development, and Analytical Research Division of Bangladesh Council of Science and Industrial Research (BCSIR), Dhaka, RUET, Rajshahi and the Department of Chemistry of Rajshahi University, Bangladesh for providing necessary facilities for proximate, TGA, CHNOS, FT-IR and other analyses.

References

[1] M.N. Islam, and F.N., Ani, "Liquid oil from fluidized bed pyrolysis of rice husk waste and its characterization", *RERIC International Energy Journal*, 20(1): pp. 55-65, 1998.

[2] Bridgwater, A.V. and Bridge, S.A., "A review of biomass pyrolysis and pyrolysis technologies", In: Bridgwater AV, Grassi G, editor. *Biomass Pyrolysis Liquids Upgrading and Utilisation*, London: Elsevier Applied Science, pp. 11-92, 1991.

[3] Soltes, E.J.,"Of biomass, pyrolysis, and liquids thereform", In: Soltes EJ, Milne TA, editor. *Pyrolysis Oils from Biomass Producing, Analyzing, and Upgrading,* Washington: American Chemical Society, pp. 1-7, 1988.

[4] Williams, P.T., Halim, S. and Taylor, D.T., "Pyrolysis of oil palm solid waste", In: Grassi G, Collina A, Zibetta H, edotor. *Biomass for Energy,Industry and Environment,* London: Elsever Applied Science, 1992.

[5] Andrews, R.G. and Patniak, P. C., "Feasibility of utilizing a biomass derived fuel for industrial gas turbine applications", In: Bridgwater AV, Hogan EN, editor. *Bio-Oil Production & Utilization*, Berkshire: CPL Press, pp. 236-245, 1996.

[6] Rick, F. and Vix, U., "Product standards for pyrolysis products for use as fuel in industrial firing plants", In: Bridgwater AV, Grassi G, editor. *Biomass Pyrolysis Liquids Upgrading and Utilisation,* London: Elsevier Science, pp. 177-218, 1991.

[7] Diebold, J. P., Milne, T. A. and Czernik, S., "Proposed specifications for various grades of pyrolysis oils", In: Bridgwater AV, Boocock DGB, editor. *Developments in Thermochemical Biomass Conversion*, London: Blackie Academic & Professional, pp. 433-447, 1997.

[8] Besler, S. Horne, P.A. and Williams, P.T., " The fuel properties of biomass derived pyrolytic oils and catalytically upgraded products", *Proc. of the 2nd World Renewable Energy Congress*, United Kingdom, pp. 1341-1345, 1992.

[9] GOB, *2006 Statistical Yearbook of Bangladesh*, Dhaka: Bangladesh Bureau of Statistics, Statistical Division of Ministry of Planning, September 2007.

[10] Islam, M.R., Nabi, M.N. and Islam, M.N., "Characterization of biomass solid waste for liquid fuel production", *Proc. of 4th Int. Conf. on Mechanical Engineering (ICME2001)*, Bangladesh, pp. 77-82, 2001.

[11] M.R., Islam, M.N. Nabi, and M.N. Islam,"The fuel properties of pyrolytic oils derived from carbonaceous solid wastes in Bangladesh". *Jurnal Teknologi*, No. 38(A); pp. 75-89; June 2003.

[12] M.R. Islam, M.N. Islam, and M.N. Nabi, "Bio-crude-oil from fluidized bed pyrolysis of rice-straw and its characterization". *International Energy Journal*, Vol. 3, No. 1; pp. 1-11; June 2002.

[13] Harker, J.H. and Bachurst, J. R., *Fuel and Energy*, London: Academic Press, 1981.

Nomenclature

Symbol	Meaning
GCV	Gross calorific value
TG	Thermogravimetric
ASTM	American society for testing and materials
GOB	Government of Bangladesh
cSt	Centistokes
pH	Negative logarithm of hydrogen ion concentration
O-H	Hydroxyl stretching
C-H	Carbon hydrogen stretching and bending

C=O	Carbonyl stretching
C=C	Carbon carbon double bonding stretching
$-N_2O$	Nitrogen dioxide stretching
C-O	Carbon oxygen stretching
FT-IR	Fourier transform infrared

Author's Guidelines for JEAS Manuscripts

Author(s) Name(s)[1]

[1]Author Affiliation(s)

E-mail

Abstract

The abstract is to be written in this location in fully-justified italicized text. Use the word "Abstract" as the title, in 12-point Times New Roman, boldface type, centered and, initially capitalized as shown above. The text should be in single spaced format with 10 point Times New Roman font. The maximum length of the abstract is to be kept within 150 words.

1. Introduction

All manuscripts must be original and written in English. These guidelines include complete descriptions of the fonts, spacing and related information for producing your journal manuscripts.
Pag Limit : Manuscript must not exceed 10 (ten) printed pages in camera ready form.

2. Formatting your paper

All printed material, including text, illustrations, and charts, must be kept within a print area of 14.96 cm wide by 24.62 cm high. Do not write or print anything outside the print area. All text must be in single space and single column format. Text must be fully justified.

3. Main title

The main title (on the first page) should begin 3.5 cm from the top edge of the page, centered. and in Times 14-point, boldface type. Capitalize the first letter of nouns, pronouns, verbs, adjectives, and adverbs; do not capitalize articles, coordinate conjunctions, or prepositions (unless the title begins with such a word). Leave two 12-point blank lines after the title.

4. Author name(s) and affiliation(s)

Author names and affiliations are to be centered beneath the title and printed in Times 12-point, non-boldface type. Affiliations of the authors are to be shown after the listing of the author names. In the case of multiple authorship, the respective affiliations are to be identified by superscript, as illustrated above. Include e-mail addresses if possible. Author information should be followed by tow 12-point blank lines.

5. Second and following pages

The second and following pages should begin 1.0 inch (2.54 cm) from the top edge. On all pages, the bottom margin should be 1-1/8 inches (2.86 cm) from the bottom edge of the page form A4 paper from the bottom edge of the page.

6. Type-style and fonts

Wherever Times is specified, Times Roman or Times New Roman may be used.

7. Main text

Type your main text in 10-point Times, single-spaced. Do not use double-spacing. All paragraphs should be indented ¼ inch (approximately 0.5 cm). Be sure your text is fully justified- that is, flush left and flush right. Please do not place any additional blank lines between paragraphs.
Figure and table captions should be 10-point Times boldface. Initially capitalize only the first word of each figure caption and table title. Figures and tables must be numbered separately. For example: "Figure 1. Title of the figure comes here.", "Table 1. Title of the table comes here." Figure captions are to be centered below the figures. Table titles are to be centered above the table.

Equations should be in 12-point, centered and numbered. The equations are to be referenced in the text as '(equation number)'.

Equation : $\rho_k(f+g) \geq \rho_k(g)$ (1)

8. First-order headings

For example, "1. Introduction", should be Times 12-point boldface, initially capitalized. flush left, with one blank line before, and one blank line after. Use a period (".") after the heading number not a colon.

Second-order headings

As in this heading, they should be Times 11-point boldface, initially capitalized, flush left, with one blank line before, and one after.

Third-order headings

Third-order headings, as in this paragraph, are discouraged. However, if you must use them, use 10-point Times, boldface, initially capitalized, flush left, preceded by one blank line, followed by a period and your text on the same line.

9. Footnotes

If possible do not use footnotes. In unavoidable case, place them at the bottom of the column on the page on which they are referenced. Use Times 8-point type, single-spaced.

10. References

List and number all bibliographical references in 9-point Times, single-spaced, at the end of your paper. When referenced in the text, enclose the citation number in square brackets, for example [1]. Where appropriate, include the name(s) of editors of referenced books.

[1] A.B. Smith, C.D. Jones, and E.F. Roberts, "Article Title", Journal, Publisher, Vol. No. pp. 1-10, Month, Year.

[2] Jones, C.D., A.B. Smith, and E.F. Roberts, Book Title, Publisher, edition, pp. year.

CONTENTS